Phase and microstructure evolutions in LC^3 binders by multi-technique approach including synchrotron microtomography

Isabel M.R. Bernal, Shiva Shirani, Ana Cuesta, Isabel Santacruz, Miguel A.G. Aranda *

Departamento de Química Inorgánica, Cristalografía y Mineralogía, Universidad de Málaga, Málaga 29071, Spain

HIGHLIGHTS

- Mechanical strength values for the studied limestone calcined clay cement with 50 wt% clinker replacement are slightly better than those derived from the neat cement after one week of hydration.
- Porosity evolution in this limestone calcined clay cement has been quantitatively measured by phase-contrast synchrotron X-ray microtomography.
- Porosity connectivities decreased from 92% at 7 hydration days to 9% at 60 days explaining the good durability properties of these binders.
- Limestone reactivity has been proved, in these aluminium-rich binders, by thermal analysis, X-ray powder diffraction coupled to the Rietveld method and synchrotron microtomography.

ARTICLE INFO

ABSTRACT

Limestone Calcined Clay Cements, LC^3, are attracting a lot of attention as it is possible to reduce the clinker factor by 50%, which means a cement CO$_2$ footprint reduction of 40%. This is compatible with maintaining the mechanical strength performances after one week, if the kaolinite contents of the raw clays are above ~40 wt%. Durability properties are also maintained or even enhanced. Here, it is used a multi-technique approach to understand the phase and microstructure developments. From the thermal analysis, partial limestone reactivity is proven. Chiefly, high-resolution synchrotron microtomography has been employed, for the first time in these systems, to characterize their microstructures. The measured total porosities, within our 1 μm spatial resolution (voxel size 0.32 μm), were 16.6, 10.0 and 2.4 vol% at 7, 8 and 60 days of hydration, respectively. Pore connectivity strongly decreases with hydration time due to the chemical reactions producing new phases filling the pores. The 6-connected porosity fractions were 92, 78, and 9% at 7, 8 and 60 days. The reactions filling the pores were investigated by Rietveld quantitative phase analysis and ^{27}Al MAS-NMR.

© 2021 The Author(s). Published by Elsevier Ltd. This is an open access article under the CC BY-NC-ND license (http://creativecommons.org/licenses/by-nc-nd/4.0/).

1. Introduction

Cement industry is a major contributor to greenhouse gases emissions as for every ton of type-I grey Portland Cement (PC), ~0.95 CO$_2$ tones are released into the atmosphere. This results into ~7% of the anthropogenic CO$_2$ emissions [1,2]. Consequently, embodied carbon content reduction of building materials has been identified as a core need in the mitigation of the consequences of the climate crisis [1,3,4]. One prominent possibility to reduce the CO$_2$ footprint of mortars and concretes is the use of supplementary cementitious materials (SCMs). These substances are being used as partial clinker substitution [5–8] or added separately in the concrete mixer [9]. SCMs have been identified by United Nations

Environment Program Sustainable Building and Climate Initiative (UNEP-SBCI) [3] as the short-term optimum strategy for lowering CO$_2$ emissions in the cement industry with the lowest economic and performance impacts.

Within the field of sustainable cements by lowering the clinker factor, Limestone Calcined Clay Cements (LC^3) are one, if not the most, promising alternative [10–12] because of their performances and the wide availability of their components. It is important that the developed SCMs have the potential of meeting high demand while yielding desired chemical, mechanical, and durability properties. Limestone and clays containing kaolinite are highly available and therefore they are suitable to face the current lack of key SCMs like reactive fly ashes and ground granulated blast furnace slag [3]. There are many studies dealing with the activation of clays for their use as SCMs [13–17]. Increasing temperature improves pozzolanic activity up to the temperature where

recrystallization, and/or the decrease in specific surface, starts to play a detrimental role [18]. The use of activated kaolinitic clays in the cement field has been very recently reviewed [19].

It has been demonstrated that LC^3 cements allow the substitution of up to 50 wt% of clinker and hence, the CO_2 footprint can be lowered by 40%; meanwhile the mechanical properties are maintained and some key durability performances like chloride resistance are improved [20–24]. LC^3 binders can yield equivalent strength to neat PC at 7 days, with a clinker substitution of 50%, if the kaolinite content of the calcined clay is larger than ~40% [10,11]. The large reactivity of metakaolin [25–27] helps to develop dense microstructures in LC^3 systems at relatively early ages. As reported in [12], there are three main reactions in LC^3 which contribute to capillary pore filling in addition to the ones taken place in the neat PCs. Firstly, the classic pozzolanic reaction, where metakaolin (MK) reacts with calcium hydroxide species (from portlandite (CH) but also from C–S–H gel, both formed by PC hydration) yielding fine particles of C–A–S–H gel [28]. Secondly, the aluminate species, mainly but not only from C_3A, react with limestone and portlandite yielding monocarboaluminate (Mc) and hemicarboaluminate (Hc) AFm-type phases [29] which as a side effect leaves more sulphates resulting in increased amounts of ettringite. Thirdly, aluminates from MK can react with calcium carbonate and CH yielding additional Hc.

Although, it is becoming clear that LC^3 binders result in dense microstructures [12,30,31], the pore properties have been studied mainly by mercury intrusion porosimetry and electron microscopy. However, and to the best of our knowledge, neither laboratory nor synchrotron X-ray microtomographies have been employed so far to study the pore structures in LC^3 binders. It must be noted that X-ray tomography is being widely used for cement-based materials [32–34], where pore descriptors (content, connectivities, etc.) have been extracted at the spatial resolution of the acquired data which ranges from ~1 μm to several dozens of μm. Thus, the main objective of this study is to characterize the pore content and pore connectivities with time using a multi-technique approach including high-resolution synchrotron X-ray microtomography.

2. Materials and procedures

2.1. Starting material

A commercial ordinary Portland cement (PC) CEM I 42.5R type was used in this study which conforms to EN 197–1. The cement was provided by Financiera y Minera S.A (Malaga, Spain) which belongs to HeidelbergCement Group.

Two different calcined clays were used. As reference, a commercial pure kaolinite, KGa-1b, purchased from The Clay Minerals Society (USA), was calcined (about 30 g per batch), in alumina crucibles at 800°C for 1 h to produce high purity metakaolin (MK); crucibles (8 cm upper-diameter) were filled up to ~3 cm. Milling was not needed. Approximately 20 kg of kaolinite-rich clay, reference FC-35, was provided by Caolines de Vimianzo, S.A.U. (A Coruña, Spain). The Rietveld plot and the thermal analysis traces for the as-received clay are shown in Supporting Information, Figs. S1 and S2, respectively. This clay was concluded to have ~75 wt% of kaolinite (within the variability of this industrial material and the accuracies of the employed analytical techniques). A small amount of this clay, which was used to perform microtomography studies, was calcined at 800°C as described for the kaolinite used as reference. The as-received clay pellets were disc-milled for 3 min (in batches of 50 g) prior to calcination. The same alumina crucibles were also filled up to ~3 cm. The laboratory-calcined clays were not further milled. A much larger fraction, 20 kg, was calcined

in a brick-maker Malaga's company, Inducerama S.L. in a large industrial oven with a maximum temperature of 860°C and a total residence time of 3 h. Ceramic containers were used for calcination, where the thickness of the layer of clay powder was 3–4 cm. A total of 3 calcination batches were needed. The calcined clays were analysed by LXRPD and after that, mixed in a big container for 30 min. Both as-received pellets and calcined clay were ground in a Micro-Deval ball mill (Proeti) at 100 rpm, in batches of 1.5 kg for 30 min, until the target particle size was obtained. The X-ray diffraction pattern of this calcined (activated) clay is shown in Fig. S3. This calcined sample was used for the remaining characterisation techniques.

An industrially-available limestone (LS) with a high content of calcium carbonate was selected to prepare the LC^3 blends. This material came from the quarry of Financiera y Minera S.A and it was disc milled for 3 min in batches of 100 g, up to a total of 5 kg. Gypsum was provided by Hormigones y Cementos Andaluces S.L. The chemical [by X-ray fluorescence (XRF)] and phase [by laboratory X-ray powder diffraction (LXRPD) using the Rietveld method] compositions are shown in Table 1. The particle size distribution (PSD) of the starting materials, measured by laser diffraction, is shown in Fig. 1. A summary of the textural parameters including size distribution percentiles for all employed powders, Blaine values, and specific surface areas are given in Table 2.

Hereafter, cement nomenclature will be adopted: C = CaO, S = SiO_2, A = Al_2O_3, F = Fe_2O_3, c = CO_2, s = SO_3 and H = H_2O. Thus, for example, Ca_3SiO_5 is denoted as C_3S and $CaCO_3$ as Cc. Furthermore, ettringite ($Ca_6Al_2(SO_4)_3(OH)_{12}\cdot26H_2O$), Kuzelite ($Ca_2Al(OH)_6[(SO_4)_{0.5}3H_2O]$) and Hemicarbo-aluminate ($Ca_2Al(OH)_6[(CO_3)_{0.25}OH_{0.5}2H_2O]$) are abbreviated as AFt, AFm and Hc, respectively.

2.2. Mixture design

Two blends were designed for this study:

The PC-FC35-Cc-G system contained 52 wt% of PC, 30 wt% of the calcined clay (FC-35), 15 wt% of limestone, and 3 wt% of gypsum.

The PC-MK-G system had 67 wt% of PC, 30 wt% of MK, and 3 wt% of gypsum.

The optimum additional amount of gypsum, 3 wt%, was determined by calorimetry, as shown in Supporting Information, Fig. S4. For the synchrotron study, the dry mixtures were produced by manually mixing the raw materials for 15 min using an Agatha mortar. For the laboratory studies, 2 kg of PC-FC35-Cc-G blend was prepared using a Micro-Deval mill (Proeti) in 2 cycles of 30 min.

Table 1
Chemical compositions for Portland cement, FC35 clay, kaolinite, and limestone*.

	PC	FC35	Kaolinite	LS
CaO	62.89	0.11	0.08	54.54
SiO_2	19.75	54.54	53.20	0.06
Al_2O_3	4.98	42.07	46.49	0.03
Fe_2O_3	3.41	1.46	0.34	0.01
Na_2O	0.30	0.06	0.00	0.00
K_2O	1.05	2.33	0.04	0.00
TiO_2	0.25	0.12	1.84	0.00
MgO	1.53	0.15	0.00	0.34
P_2O_5	0.11	0.11	0.05	0.01
SO_3	3.37	0.09	0.03	0.01
LOI	2.72	13.11	13.46	43.46

* Mineralogical composition for PC (wt%): C_3S=62.1, C_2S=11.0, C_3A=7.8, C_4AF=10.7, CsH_2=0.9, $CsH_{0.5}$=2.1 and Cc=3.6. Mineralogical composition for LS (wt%): Cc=97.7 and dolomite=2.3.
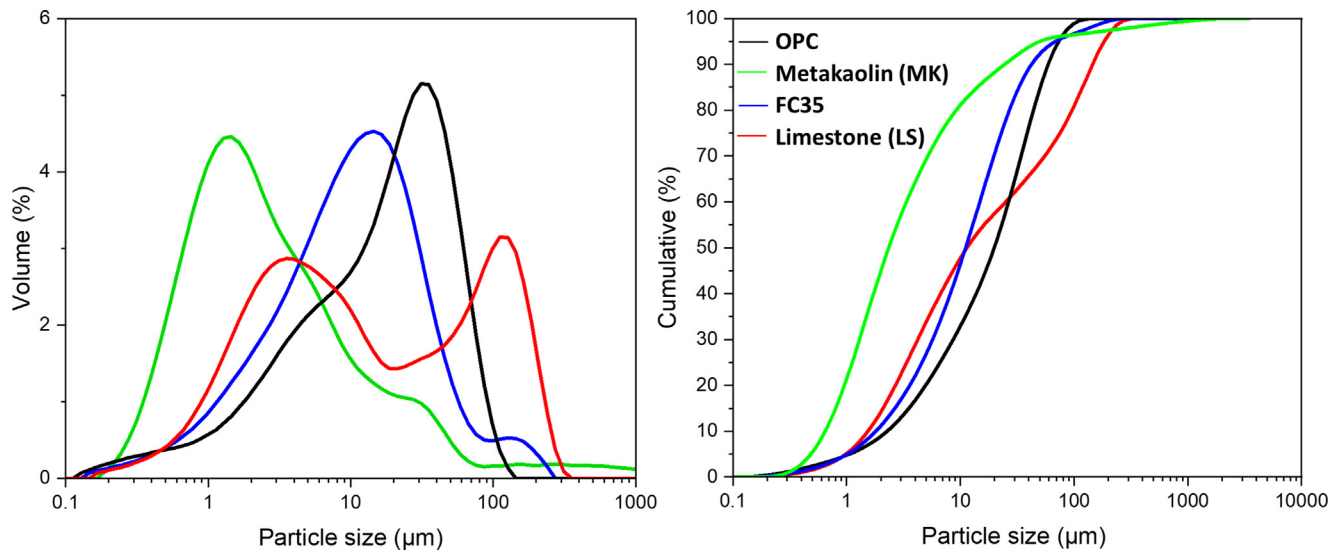
Fig. 1. (Left) Particle size distribution of materials employed in this work. (Right) Cumulative curves.

Table 2
Particle size (D_{v10}, D_{v50}, and D_{v90}), span (width), specific surface area and Blaine values of the employed materials in this work.

	PC	FC35-lab[$]		FC35-factory[$]			MK-lab.		LS[&]
		Stage 1[a]	Stage 2[b]	Stage 1[c]	Stage 2[d]	Stage 3[e]	Stage 1[f]	Stage 2[g]	Stage 1[h]
D_{V90} (µm)	61.9	28.3	47.8	36.6	140	42.4	10.1	24.5	146
D_{V50} (µm)	19.5	5.7	8.2	10.1	14.3	11.1	2.1	2.3	11.4
D_{V10} (µm)	2.1	1.0	1.2	1.8	2.2	1.8	0.5	0.7	1.5
Span (-)	3.1	4.8	5.7	3.4	9.6	3.7	4.6	10.2	*
SSA (m²/g)	1.2					10.3		11.6	1.6
Blaine (m²/kg)	368					567		997	580

[a] Disc milling (prior to calcination).
[b] After calcination (no additional milling required).
[c] Milling prior to calcination (Micro-Deval).
[d] After calcination (prior to milling).
[e] Milling after calcination (Micro-Deval).
[f] As-received powder.
[g] After calcination (no additional milling required).
[h] After disc milling.
[$] Received as pellets.
[&] Received as stone.
[*] Bimodal distribution.

2.3. Paste and mortar preparations

The neat PC paste used as reference was prepared with deionized water using a w/c (water-to-cement) mass ratio of 0.50. For the LC[3] mixtures, a w/b (water-to-binder) mass ratio of 0.40 was used. Moreover, to improve the workability of the PC-FC35-Cc-G mixture, 0.4 wt% (active matter referred to the binder content) of polycarboxylate-based superplasticiser, SP, (Floadis 1623, with 25 wt% of active matter, Adex Polymer S.L., Madrid, Spain) was used; the water added with the SP was considered for w/b content calculations.

Pastes were mechanically stirred for 90 s at 800 rpm, with 30 s pause, followed by another 90 s stirring at 800 rpm, to improve their homogeneity. Then, the pastes were poured into hermetically closed cylinders of polytetrafluoroethylene (PTFE), and rotated during the first 24 h (16 rpm) at 20°C. Subsequently, cylinders were taken out and samples were kept submerged in water at the same temperature for 2, 7, 28, and 60 days. Prior to LXRPD analysis, samples were manually ground and mixed with 15 wt%

of quartz as the internal standard. The hydration of these pastes was not further stopped unless specified.

The hydration of the pastes was stopped for the thermogravimetric analysis in order to determine the free water content. For this study, samples were manually ground, filtrated in a Whatman system and washed twice with isopropanol, and once with diethyl ether.

For the microtomographic experiment, fresh pastes were directly loaded into glass capillaries of 0.50 mm diameter with a syringe. The capillaries were sealed with grease to avoid any water loss. Capillaries were rotated during the first 24 h. Data were collected at 7, 28, and 60 days of hydration without any additional sample preparation step to preserve the microstructures.

Standard mortars were cast to determine the flexural and compressive strength developments of the reference neat PC and PC-FC35-Cc-G blend. CEM I 42.5R mortars were prepared according to EN196-1 at cement/sand and w/c ratios of 1/3 and 0.5, respectively. For the sake of comparison, a second set of mortars were prepared with w/c ratio of 0.40. For the LC[3] blend, a w/b mass ratio

of 0.40 was used and a 0.4 wt% of the same superplasticiser (active mater referred to blend) was added. Prisms with dimensions ($40 \times 40 \times 160$ mm^3) were cast and then de-aired in a jolting table (Ibertest, model IB-32-0 45E, 2002) with a total of 120 knocks. Moulds were half cast and knocked for 60 times for a better homogenization. After that, they were fully cast and other 60 knocks were carried out. The prisms were kept at 20°C and 99% RH for 24 h. Subsequently, they were unmoulded and cured in a fog room at 20°C until tested.

3. Analytical techniques

3.1. Compressive and flexural strengths

Mechanical strength properties of PC and PC-FC35-Cc-G mortars were measured at 20°C in a press (Model Autotest 200/10 W, Ibertest, Madrid, Spain) according to EN196-1 and at a rate of 1.5 MPa·s^{-1}, at 2, 7 and 28 days of hydration. The reported flexural values are the average of three broken prisms. The reported compressive values are the average of six measurements.

3.2. Textural characterisation

The specific surface areas were measured by multi-point N_2 adsorption with a BET (Brunauer–Emmett–Teller) (ASAP 2420, Micromeritics, USA) instrument. The fineness was measured in a Blaine fineness apparatus (Controls) according to UNE-EN 196–6. The particle size distributions were measured by laser diffraction (MasterSizerS, Malvern, provided with a dry chamber).

3.3. X-ray fluorescence analysis

The elemental compositions were measured using an PANalytical Axios max advanced equipment at Financiera y Minera S.A. (Málaga).

3.4. Laboratory X-ray powder diffraction

LXRPD data for all the samples were collected on a D8 ADVANCE (Bruker AXS) diffractometer (SCAI – Universidad de Málaga) in transmission geometry (θ/θ) which is equipped with a Johansson monochromator, using strictly monochromatic Mo-Kα_1 radiation, λ = 0.7093 Å. Rietveld analyses were performed using the GSAS suite of programs and the EXPGUI graphic interface [35]. Final global optimised parameters were: background coefficients, zero-shift error, cell parameters, and peak shape parameters using a pseudo-Voigt peak shape function. The cement pastes were mixed with 15 wt% of quartz as the internal standard. Thus, the ACn (amorphous and crystalline non-determined) contents were determined by the internal standard methodology [36].

3.5. Thermal analysis (TA)

Differential thermal analysis (DTA) and thermogravimetric analysis (TGA) measurements for the pastes were performed in a SDT-Q600 analyser from TA instruments (New Castle, DE). The temperature was varied from RT to 1000°C at a heating rate of 10°C/min. Measurements were made in open platinum crucibles under synthetic air flow. The weighed loss from RT to 550°C was assigned as chemically bound water and the weighed loss from 550 to 1000°C was considered as CO_2. The free water content (FW), in wt%, was calculated for each paste using the total added water and the bound water as reported in [37].

3.6. Isothermal calorimetry

Data were acquired in an eight channels Thermal Activity Monitor (TAM) instrument using glass ampoules. The paste preparation was carried out outside the calorimeter by mixing the cements with water and shaking for one minute manually and then during another minute with a vortex mixer. After homogenisation, the pastes were inserted into the ampoules and located within the calorimeter. The heat flow curves were collected after 45 min of mixing, to allow temperature stabilisation, up to 7 days at the target temperatures.

3.7. ^{27}Al magic angle spinning nuclear magnetic resonance (MAS-NMR)

The ^{27}Al spectra were recorded at RT in an AVANCEIII HD 600 (Bruker AXS) spectrometer using a triple resonance DVT probe of 2.5 mm at a spinning rate of 20 kHz. The magnetic field was 14.1 T corresponding to a ^{27}Al resonance frequency of 156.37 MHz. The chemical shifts are referenced to Al(NO$_3$)$_3$. ^{27}Al MAS NMR spectra were recorded with an excitation pulse of 0.29 μs and 1 s delay without ^1H decoupling (^{27}Al One pulse) and summing up 2000 scans.

3.8. Mercury intrusion porosimetry (MIP)

Pore entry size distributions were measured on cylindrical samples of dimensions: 1 cm of diameter and 1.5 cm of height. Two pieces of each paste were independently measured, and the reported data are the average of the two traces which were very similar. The pastes were cured for 7 and 28 days following the procedure described above. Before MIP measurements, the hydration was stopped by sinking the pieces in isopropanol for 3 days. Then, the pastes were dried by gentle heating at 40°C up to constant weight, which took about 5 days. In order to measure porosity in the range from 1 mm down to 4 nm (radius), a micromeritics AutoPore IV 9500 porosimeter (Micromeritics Instrument Corporation, Norcross – GA, US) was used. The pressure applied by the intrusion porosimeter ranged from 0 to 206 MPa in step mode. A constant contact angle of 140° was assumed for data evaluation [38].

3.9. Field emission gun-scanning electron microscopy (FEG-SEM)

PC-FC35-Cc-G paste hydrated at 28 days was characterised by Back Scattered Electron (BSE) combined with Energy-dispersive X-ray spectroscopy (EDS) using a FEG-SEM microscope (FEI, Helios Nanolab 650). BSE images were taken at 15 kV with a retractable concentric backscatter (CBS) detector that is an annular solid-state device. EDS analysis was carried out with a X-Max 50 mm^2 silicon drift detector (Oxford Instruments) with AZtec software (v.1.0). A dwell time of 30 μs was used. 500 points were analysed of five different areas. Prior to microscopy characterisation, the paste was embedded in epoxy resin, polished with diamond down to 3 μm, and iridium sputtered.

3.10. Synchrotron microtomography study

Microtomographic data were taken at TOMCAT beamline (Swiss Light Source, Paul Scherrer Institut, Switzerland) for PC-FC35-Cc-G pastes hydrated for 7, 28, and 60 days. The scans were acquired with an X-ray beam of 15 keV and a sample-to-detector distance of 5.5 mm, to obtain high contrast between the different main components but avoiding mutliple fringes. The detector system was a 20-μm thick LuAG:Ce scintillator, a diffraction limited microscope optics, 20× objective, and a high-resolution CCD camera (pco.edge 5.5, PCO AG, Germany). This high-resolution experimen-

tal setup yielded an isotropic pixel size of 0.325 μm and a field of view of 0.8×0.7 mm (V × H) which was large enough to image the whole width of a capillary, ϕ = 0.5 mm. The recording time for each frame was 200 ms. For each tomogram, 1501 projections over 180° sample rotation were taken resulting in a total scan time of 5 min per dataset. Phase retrieval of the projections was performed using the Paganin algorithm [39] and then tomographic reconstructions were carried out [40]. Image analysis and interpretation, including the labeling of all image voxel into their constituent phases, were performed with Dragonfly software (version 2020.2, Object Research Systems (ORS) Inc., Montreal, Canada). For the segmentation of the main components, a large Volume of Interest (VOI) of ~1×10^8 μm^3 size was evaluated. A simple cylinder mask was used to exclude the sample holder capillary walls from the analysis.

4. Results and discussion

4.1. Mechanical strengths

The mechanical strength results for the LC^3 and the reference PC mortars are displayed in Fig. 2. At 2 days, and as expected, the strength values of the PC-FC35-Cc-G blend are smaller than those of the neat PC reference with both w/c ratios. At this very early age, the compressive strength of the LC^3 binder was 27% and 44% lower than those of PC with w/c ratios of 0.50 and 0.40, respectively. This is justified mainly because the much lower clinker content and the pozzolanic reaction is just starting. It is explicitly acknowledged that the possible retarding effect of the employed superplasticiser has not been investigated and this merits further research.

At 7 days, the compressive strength of the LC^3 mortar was similar to that of PC with w/c = 0.4 and 26% larger than that of PC with w/c = 0.50, see Fig. 2. Furthermore, at 28 days of hydration the compressive strength values were 62(1), 58(1) and 52(1) MPa for PC-FC35-Cc-G and PC w/c = 0.40 and w/c = 0.50, respectively. Therefore, the LC^3 binder showed a 7% and 19% increase in strength respect to the neat PC binders. The flexural strength development fully mirrors the compressive strength trend, see Fig. 2b. Hence, and as previously reported [10,11], it is possible to have a 50% clinker factor reduction and to improve mechanical strength performances after one week.

Once it was shown that the LC^3 system displays the expected mechanical properties, the porosity evolution was analysed by MIP and chiefly by synchrotron microtomography. However, for an adequate understanding, a prior step is needed where the phase development is characterised as this indirectly determines porosity progress.

4.2. Calorimetric study

The heat flow and cumulative heat curves of the studied LC^3 systems are shown in Fig. 3. In addition to the PC-FC35-Cc-G and PC-MK-G blends, the traces for reference neat PC are also given. As the dissolution peak is not recorded with our employed experimental procedure, the alite dissolution peak, with its associated C-(A)-S-H gel precipitation and CH crystallisation, is the first one measured by calorimetry, shown in Fig. 3a. It can be seen that the first hydration peak takes place at 11.0 h in the neat PC and it is slightly accelerated in the PC-MK-G blend to 8.0 h and retarded to 18.1 h for PC-FC35-Cc-G. Calorimetry is a very simple and useful technique to evaluate if the sulphate content is adequate. It has been previously reported [41] that the sulphate content in LC^3 system should be adjusted so that the aluminate (second) peak takes place after the alite peak when gypsum is exhausted. This second peak, highlighted in Fig. 3a, is due to the fast dissolution of C$_3$A and crystallisation of ettringite from the desorption of sulphate anions from C-(A)-S-H gel. This second peak takes place at ~18.5 and ~46 h for PC-MK-G and PC-FC35-Cc-G, respectively. Their positions, well after the first peak, indicating that the samples are properly sulphated and therefore worth being further investigated. The third hydration peak, see Fig. 3a, is significantly larger in LC^3 systems than in neat PC pastes and it has been reported to take place between 48 and 96 h of hydration [12]. This peak is usually associated with the formation of AFm phases, including those containing carbonate anions, and its position and intensity were reported to be highly depended on the MK content [12]. Fig. 3a revealed that the third peak took place at ~50 and ~85 h for PC-MK-G and PC-FC35-Cc-G, respectively. This is in full agreement with a very recent report [12].

The cumulative heat traces are shown in Fig. 3b. The dilution with 15 wt% of limestone in PC-FC35-Cc-G is reflected in the lower heat developed after 7 days of hydration, when referred to the whole amount of solid. In any case, it is noted that this sample developed only 223 J/g of binder, see Fig. 3b, but its mechanical strength performances are very good, see Fig. 2. PC-MK-G has a 30 wt% of MK and not dilution with limestone and therefore, its cumulative heat at 7 days is larger 272 J/g of binder. The role of calcite will be further investigated in the subsections below. Just for reference, the neat PC paste (with w/c = 0.50) developed 310 J/g at 7 days of hydration.
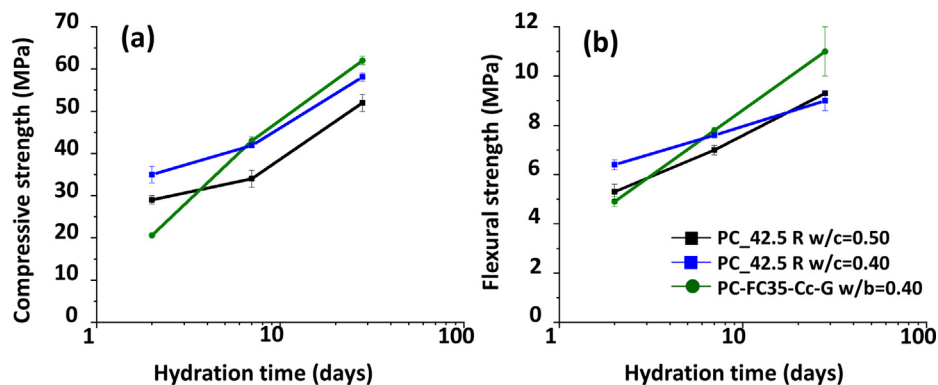

Fig. 2. Mechanical strength data for PC with w/c = 0.50 (black), w/c = 0.40 (blue) and PC-FC35-Cc-G w/b = 0.40 (green) mortars. (a) Time evolution of the compressive strength. (b) Time evolution of the flexural strength. (For interpretation of the references to colour in this figure legend, the reader is referred to the web version of this article.)
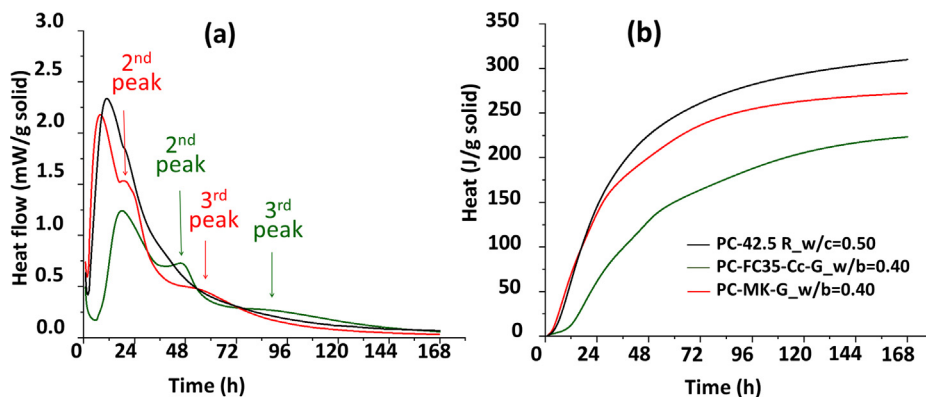
Fig. 3. Calorimetric study up to 7 days for the studied cement pastes. (a) Heat flow. (b) Cumulative heat. The position of the second and third hydration peaks in LC^3 systems are highlighted.
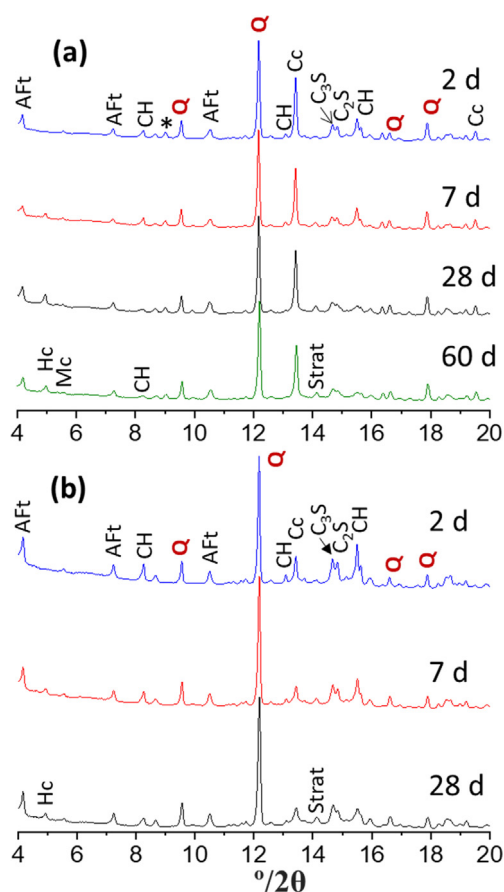

Fig. 4. Laboratory X-ray powder diffraction patterns (Mo-Kα_1, λ = 0.71 Å) for PC-FC35-Cc-G (a) and PC-MK-G (b) pastes as a function of hydrating time. The main peaks are labelled following the cement notation, including those of the internal standard (Q). The start denotes a peak (muscovite) coming from the employed (calcined) clay.

4.3. Laboratory X-ray powder diffraction study

The pastes were mixed with quartz, used as an internal standard, to find out the overall amorphous and crystalline-non-determined (ACn) content, [36,42]. Fig. 4 displays the raw powder patterns collected at 2, 7, 28, and 60 days for PC-FC35-Cc-G and at

2, 7, and 28 days for PC-MK-G in order to do an initial qualitative assessment.

Powder pattern for PC-FC35-Cc-G at 2 days already shows a relatively large amount of ettringite, see Fig. 4a. It must be noted that portlandite content is quite low which means that pozzolanic reaction is already taken place. It must be also noted that mono- and hemi- carbonate AFm phases have still not been formed, in agreement with the calorimetric study discussed just above. The most important qualitative observations with time are: i) the development of Hemicarbonate (Hc) which importantly contribute to the pore refinement as very recently shown [12]; ii) the presence of crystalline monocarbonate (Mc) is negligible; and iii) the low amount of crystalline portlandite which indicate the progression of the pozzolanic reaction which is also key for the decreasing of pore fraction and pore connectivities. The corresponding powder patterns for PC-MK-G are shown in Fig. 4b. The main difference between the two series is the limestone content as in this case is just ~2 wt% coming from the employed PC. As expected, for this series, the Hc content is much smaller.

The seven LXRPD data have been analysed by the Rietveld method, to obtain quantitative phase analyses (RQPA). The Rietveld plots are shown in Figs. S5 and S6 for the pastes PC-FC35-Cc-G and PC-MK-G, respectively. The resulting contents are summarised in Table 3. The hydration degrees increased with time as expected. The reaction degree of C$_3$S at 20°C and 28 days was ~92% and ~84% for PC-FC35-Cc-G and PC-MK-G, respectively. Furthermore, at two days the C$_3$S reaction degrees were 74% and 67%. This indicates that C$_3$S hydration is faster in PC-FC35-Cc-G. We speculate that this enhanced reactivity could be due to the presence of calcite which yields extra (suitable) surface for C-S-H precipitation. However, more research is needed to fully establish this point. Conversely, the reaction degree of belite at 28 days was negligible for both samples. This is likely due to the slow hydration kinetics of belite, with the lack of space for product crystallization at later hydration ages, due to the employed w/b ratio, also playing a role. Very interestingly, the tetracalcium ferroaluminate reaction degree at 28 days was much larger for PC-FC35-Cc-G, ~72%, than for PC-MK-G, which was ~35%. A similar trend was found for C$_3$A, which highlights the importance of limestone in increasing the reactivity of the aluminate phases, in agreement with previous publications [12,29]. Finally concerning the phases of the cement, at 28 days it remains 8.2 g out of the initial 34.1 g, yielding an overall 76% of reaction for the four main clinker phases in PC-FC35-Cc-G. The same simple calculation for PC-MK-G gave 14.6 g out of the initial 43.8 g meaning an overall 67% degree of reaction, see Table 3. This shows that calcite enhances the reaction rate of the clinker phases

Table 3

Mineralogical composition (wt%) for the pastes determined by RQPA, including the ACn (overall amorphous content) and FW (free water) from the thermal study.

Phases	t_0[a]	PC-FC35-Cc-G				t_0[b]	PC-MK-G		
		2d	7d	28d	60d		2d	7d	28d
C_3S	23.1(2)	6.1(6)	3.4(6)	1.9(4)	1.9(3)	29.7(2)	9.6(7)	5.4(5)	4.9(5)
C_2S	4.1(7)	5.7(9)	6.1(9)	5.4(7)	5.6(7)	5.3(7)	7.5(7)	7.0(8)	5.1(7)
C_3A	2.9(3)	0.9(2)	0.4(2)	–	–	3.7(3)	2.5(3)	1.7(3)	1.4(2)
C_4AF	4.0(3)	1.4(2)	1.4(2)	1.1(2)	1.1(1)	5.1(3)	4.3(6)	3.6(4)	3.3(4)
Cc	12.0(2)	12.6(4)	13.5(4)	11.6(4)	11.4(3)	1.7(2)	1.7(2)	1.0(2)	1.0(1)
AFt	–	7.5(6)	4.0(6)	7.5(6)	7.3(6)	–	12.1(7)	9.7(6)	10.5(5)
CH	–	3.4(2)	3.7(2)	0.6(1)	0.6(1)	–	5.3(3)	3.2(2)	1.7(2)
AFm	–	–	–	–	–	–	–	–	–
Strat		2.0(5)	4.1(9)	4.0(9)	3.3(9)	–	3.1(7)	4.5(1.0)	3.6(9)
Hc		–	1.3(4)	3.5(4)	2.8(4)	–	–	1.4(3)	1.3(3)
ACn	21.4*	43.0	46.8	55.9	58.3	21.4*	41.9	50.2	60.2
FW	28.6	17.3	15.2	8.5	7.6	28.6	12.1	12.2	7.0

[a] This binder also contains at t_0: 2.4 wt% of gypsum, 0.8 wt% of basanite, 0.5 wt% of K_2SO_4 and 0.2 wt% of aphthitalite

[b] This binder also contains at t_0: 2.5 wt% of gypsum, 1.0 wt% of basanite, 0.7 wt% of K_2SO_4 and 0.2 wt% of aphthitalite

* Nominal amount of calcined clay added.

in the employed conditions. We do not discuss here the calcite dissolution, from RQPA, as its accurate quantification is complicated because of the overlapping of the main diffraction peaks and mainly because of its variable preferred orientation along [104] direction. This will be discussed in the thermal analysis subsection but the data given in Table 3 are compatible with partial reactivity.

Concerning the hydrated phases, some observations can be highlighted. Firstly, Hc was the main carbonate-containing AFm phase and, as expected, its amount at 28 days was higher in PC-FC35-Cc-G, 3.5 wt%, than in PC-MK-G, 1.3 wt%. Secondly, stratlingite (another AFm-type phase, C_2ASH_8) is formed in both systems, ~4 wt%, as expected in a aluminate-rich environment. Thirdly, AFt content at 28 days in PC-MK-G, 10.5 wt%, is larger than that present in PC-FC35-Cc-G, 7.5 wt%. Fourthly, the C-(A)-S-H content, which is the main fraction of the amorphous component, is very large in both binder, being 57 and 60 wt% for PC-FC35-Cc-G and PC-MK-G, respectively. Fifthly, the portlandite contents are very low and decrease with time due to the pozzolanic reaction. Finally, the free water content, determined from thermal analysis as described in the experimental section was quite low already at 28 days of hydration, 8.5 and 7.0 wt% for PC-FC35-Cc-G and PC-MK-G, respectively.

4.4. Thermal analysis study

Fig. 5 shows the thermal traces for PC-FC35-Cc-G and PC-MK-G pastes as a function of the hydration time. The individual thermal plots are given in S.I., Figs. S7 and S8. On the one hand, the portlandite contents determined using the tangential method [43] are in full agreement with the RQPA values, given in Table 3. For PC-FC35-Cc-G, they were 3.7, 3.0, 0.8, and 0.3 wt% at 2, 7, 28, and 60 days of hydration. The portlandite contents for PC-MK-G were 4.3, 3.3, and 1.7 wt% at 2, 7, and 28 days. In addition, the $CaCO_3$ contents for PC-MK-G, also derived by the tangential method, were 1.7, 1.4 and 1.2 wt% at 2, 7, and 28 days, respectively. These low values came just from the PC used, see Table 3. For PC-FC35-Cc-G, the $CaCO_3$ contents were 12.5, 11.6, 10.2, and 9.3 wt% at 2, 7, 28, and 60 days of hydration, respectively, see Fig. 5a. The reaction degree of calcite is larger than that justified by the crystallisation of Hc phase, see just above. Therefore, it is concluded that a significant fraction of CO_3^{2-}-containing phase(s) precipitate as amorphous or nanocrystalline. A ptychographic synchrotron experiment is planned to clarify this issue. In any case, the smooth and constant decrease in the $CaCO_3$ contents with hydration time confirms the reactivity of calcite in the presence of the MK-rich cal-
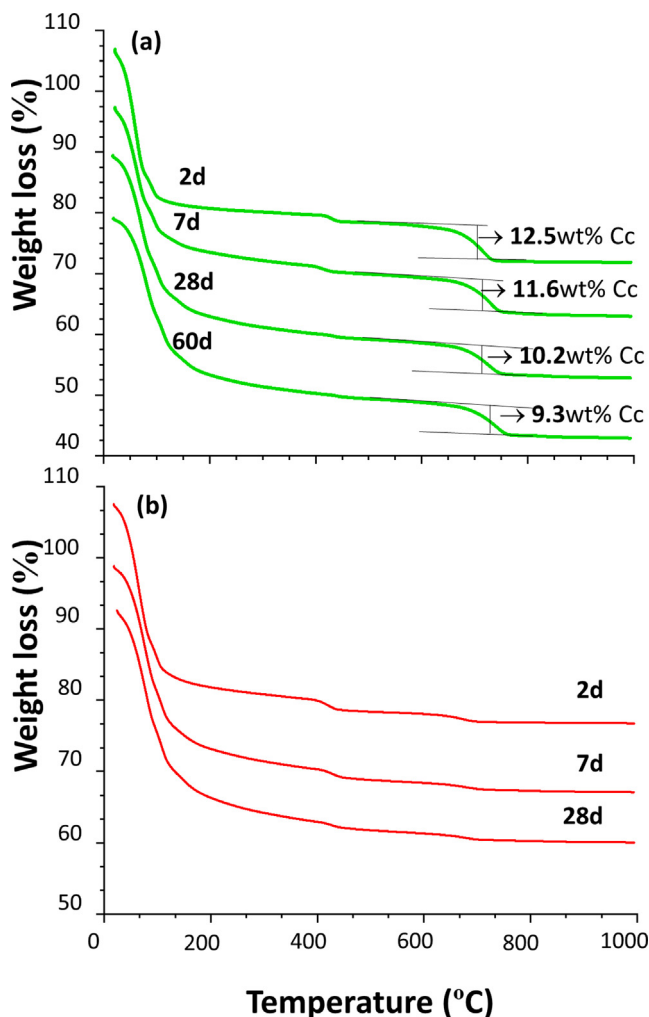

Fig. 5. Thermal analysis data for (a) PC-FC35-Cc-G and (b) PC-MK-G pastes as a function of hydrating time. The amounts of $CaCO_3$ were determined by the slope methods and they are explicitly given. The traces have been displaced vertically for better visualization.

cined clays and its key role for AFm-type phase(s) formation. This role is in addition to its general property of providing a further surface for C-(A)-S-H gel nucleation sites.
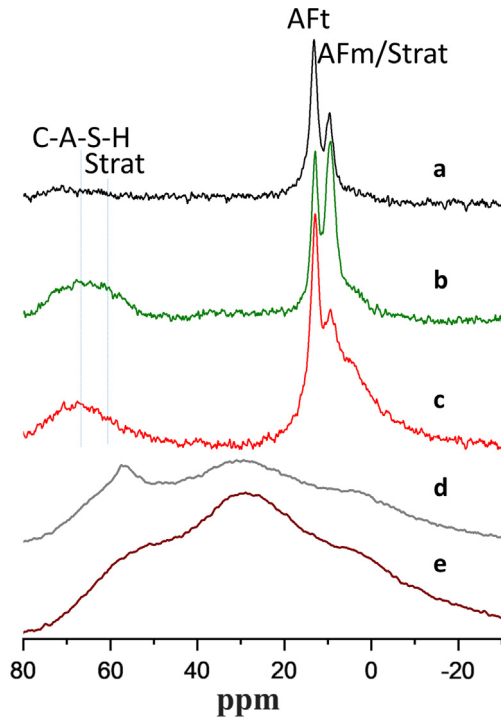
Fig. 6. ^{27}Al MAS-NMR spectra for studied samples, in the case of pastes they were hydrated for 28 days at 20°C. (a) PC-42.5 R w/c = 0.50, (b) PC-FC35-Cc-G w/b = 0.40 (c) PC-MK-G w/b = 0.40, (d) FC35 clay calcined at 860°C, and (e) Metakaolin (from kaolinite calcined at 800°C).

4.5. ^{27}Al MAS-NMR study

Fig. 6 displays the ^{27}Al MAS-NMR spectra for the studied pastes at 28 days of hydration: PC-FC35-Cc-G, PC-MK-G and PC-42.5R

(used as reference). Moreover, this figure also shows the spectra for the FC35 and MK calcined clays. The anhydrous samples show the presence of a main broad band centred at ~30 ppm (AlO$_5$ environment) with two shoulders at ~55 (AlO$_4$ species) and ~5 ppm (AlO$_6$ groups), see Fig. 6d and e. The absence of the main resonance, at ~30 ppm, in the hydrated samples, PC-FC35-Cc-G and PC-MK-G, indicates nearly full consumption of MK at 28 days of hydration. The spectrum for the PC paste, see Fig. 6a, shows two sharp bands. One is located at 13.2 ppm and is due to the Al within AFt phase and a second one is located at 9.4 ppm which corresponds to AFm, in agreement with previous publications [44]. The spectrum for PC-FC35-Cc-G shows the AFt and AFm/stratlingite (octahedrally-coordinated aluminium) resonance bands at 12.9 and 9.3 ppm, respectively. Additionally, the broad band centred at ~65 ppm is due to the tetrahedrally-coordinated aluminium which is located within the silicate chains of the gel giving rise to C-A-S-H gel [45,46]. The spectrum for PC-MK-G is very similar to that of PC-FC35-Cc-G paste, with resonance bands at 13.0 and 9.4 ppm, although it also contains a more pronounced band around 4.5 ppm and very commonly referred to as "third aluminate hydrate" [46]. Very recently it has been demonstrated that is phase likely does not exist and that this resonance is most probably due to bridging Al(VI) species which behave as network formers in C-A-S-H [47]. It is worth noting that that stratlingite can only be clearly identified by ^{27}Al MAS-NMR from its resonance located ~60 ppm, corresponding to the interlayer tetrahedral Al [46,48], as the octahedral Al resonance overlaps with that of the AFm phase. Although, the presence of stratlingite in PC-FC35-Cc-G and PC-MK-G pastes has been confirmed by LXRPD, ^{27}Al MAS-NMR spectra did not clearly show this resonance likely due to its low intensity and being partly overlapped with that of C-A-S-H.

4.6. Mercury intrusion porosimetry study

The entry pore size distributions and cumulative porosities for PC-FC35-Cc-G and PC-MK-G pastes cured at 7 and 28 days are
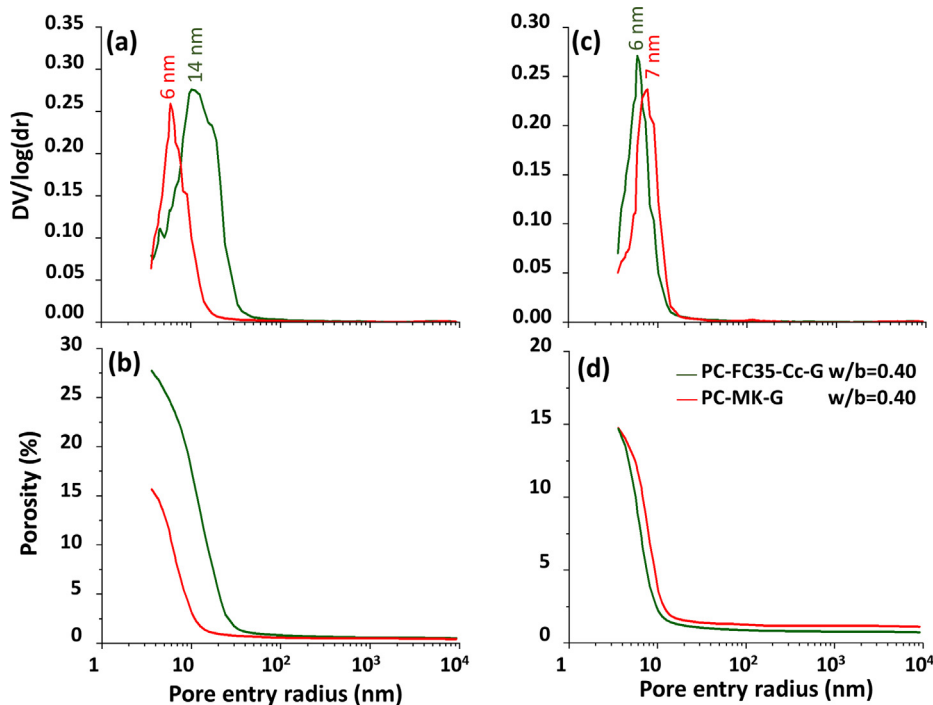

Fig. 7. Textural details, as measured by mercury intrusion porosimetry, for pastes cured at 20°C. Differential pore entry size distributions: panels (a) and (c) for curing times of 7 and 28 days, respectively. Cumulative porosity curves: panels (b) and (d) for 7 and 28 days, respectively.

shown in Fig. 7. As mercury only intrudes through connected porosity, it results in an underestimation of the volume of the biggest pores, known as ink-bottle effect. This feature makes the direct comparison of MIP data with results from other techniques difficult but the evolution within series and the comparison between series with data taken under the same experimental conditions is quite informative.

The critical pore entry radii for PC-FC35-Cc-G and PC-MK-G pastes at 7 days were 14 and 6 nm, respectively, see Fig. 7a. It is worth noting that the pore radius for the MK paste was already very small at one week. In addition, the critical pore entry radii for the two studied pastes at 28 days were quite similar, within the variability of the measurements, 7 nm, see Fig. 7c. These data indicate that pore refinement in this time frame has taken place for PC-FC35-Cc-G but not for PC-MK-G. This is fully in line with the previous characterization as during this period FW evolved from ~15% to ~9% for PC-FC35-Cc-G but it stays nearly constant at ~12% for PC-MK-G. Finally, it must be noted that the pore entry absolute values depend upon the assumed contact angle, which in this work was 140°.

The total porosities are displayed in Fig. 7b and d. At 7 days, the porosity for PC-FC35-Cc-G, was ~28%, meanwhile the porosity for PC-MK-G was ~16%. This again indicates that the rate of the hydration reaction for PC-MK-G was much faster than that of PC-FC35-Cc-G. This is very likely due to the particle size distributions, see Table 2. D_{v50} values were 11 and 2.3 μm, for the employed calcined clay and metakaolin, respectively, see also Fig. 1. The results for the studied LC^3 cement here are in line with a very recent publication reporting 30% of total porosity for a similar LC^3 paste (50% clinker replacement, w/b = 0.40, high MK content) at 7 days [12]. In addition, the total porosities for the two pastes were very similar at 28 days, ~15%, see Fig. 7d. However, it is worth noting that PC-FC35-Cc-G has an additional cement replacement of 15% by limestone. This confirms the synergic effect of limestone in the pore refinement properties of LC^3 binders [10,12,49].

4.7. BSE-SEM microscopy

PC-FC35-Cc-G paste, after 28 days of hydration, was also characterised by BSE microscopy combined with EDS. Fig. 8 shows selected EDS elemental maps of: a) combined Ca, Si and Al, b) Ca, c) Si, d) Al and e) S. Fig. S9, supporting information, displays the raw BSE-SEM image. Two pristine particles are shown, a very big one of calcite (left) and a medium size belite (right). As expected, the binder phase surrounding the two large anhydrous particles has a C-A-S-H gel composition containing also minor amounts of sulphur. The calcite particle, see Fig. 8a, presents aluminium-rich zones in it, which are highlighted with crosses, compatibles with Hc stoichiometry. Hc zones have also been identified in the upper region of the calcite particle, see Fig. 8a. The presence of Hc zones are in agreement with the reactivity of calcite determined by thermal analysis (above) and synchrotron microtomography (see below).

4.8. Synchrotron X-ray microtomography analysis

The microstructures of the pastes have been mainly studied by synchrotron X-ray microtomography. This technique allows measuring capillaries filled with pastes without any further treatment and hence it is possible to avoid microstructure alteration due to sample preparation. Furthermore, the coherence properties of the synchrotron X-rays were employed by placing the detector 5.5 mm far from the sample which resulted in the edge enhancement also known as X-ray phase-contrast [39]. From a single propagation-based acquisition, two data sets were reconstructed: (i) without Paganin algorithm applied (hereafter, absorption data) and (ii) with Paganin algorithm applied (hereafter, Paganin data) [39]. Fig. 9 displays representative tomographic slices showing glass capillary cross sections (Paganin data) for the PC-FC35-Cc-G pastes hydrated during 7, 28, and 60 days at 20°C. For the sake of comparison, the same tomographic slice (absorption data) for PC-FC35-Cc-G hydrated for 7 days is also shown. In both reconstructions, the anhydrous cement particles (highly absorbing) are whiter and the porous regions (air and water) are darker, the hydrated phases and limestone having intermediate grey-scale values. However, it can also be observed that the image contrast (information) in the Paganin reconstructed tomograms is larger because the differences in grey-scale values of the different components are wider. Therefore, in the remaining part of this work, only the Paganin data will be analysed/discussed.
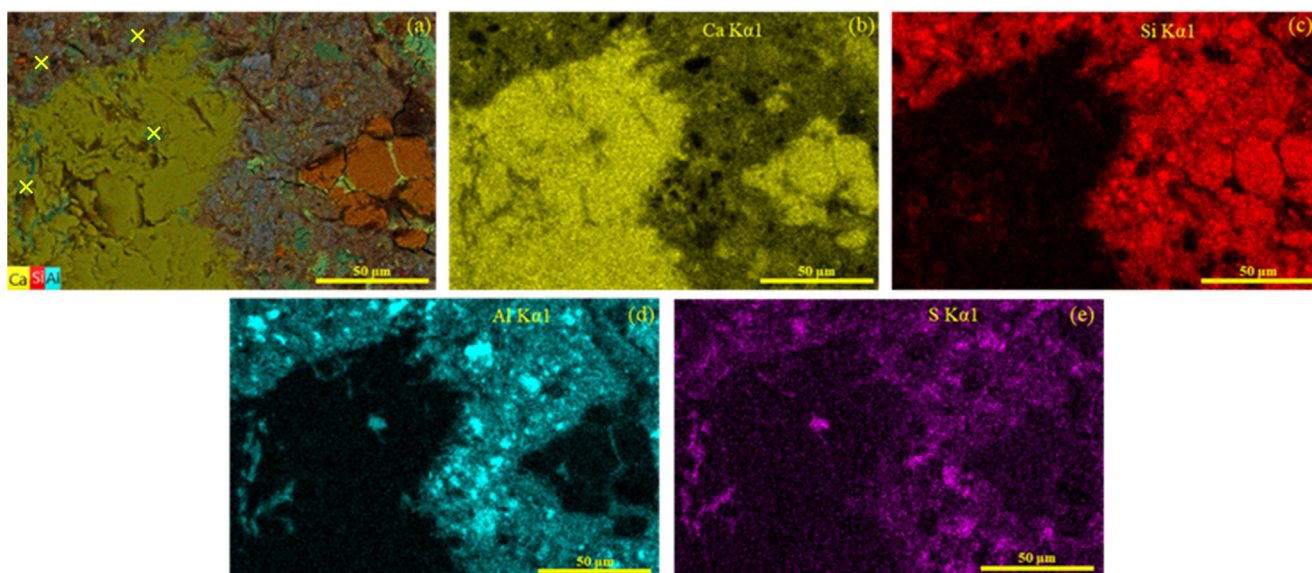

Fig. 8. BSE-EDS elemental maps for PC-FC35-Cc-G paste after 28 days of hydration. a) combined Ca, Si and Al, b) Ca, c) Si, d) Al and e) S. The yellow crosses highlight regions with Hc-compatible stoichiometries. (For interpretation of the references to colour in this figure legend, the reader is referred to the web version of this article.)
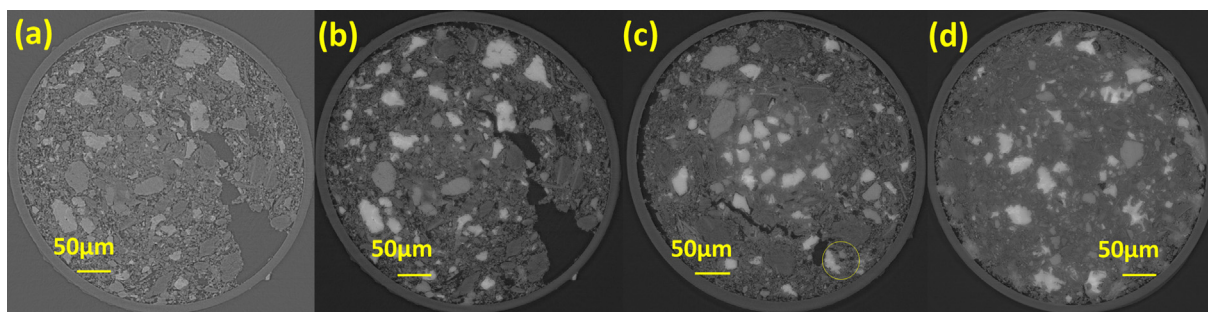
Fig. 9. Reconstructed tomographic slices for the PC-FC35-Cc-G pastes as a function of curing time. (a) Slice without applying Paganin algorithm for PC-FC35-Cc-G-7d. (b) Same slice than (a) but applying the Paganin algorithm. The slices for PC-FC35-Cc-G-28d and PC-FC35-Cc-G-60d applying Paganin are displayed in panels (c) and (d), respectively.
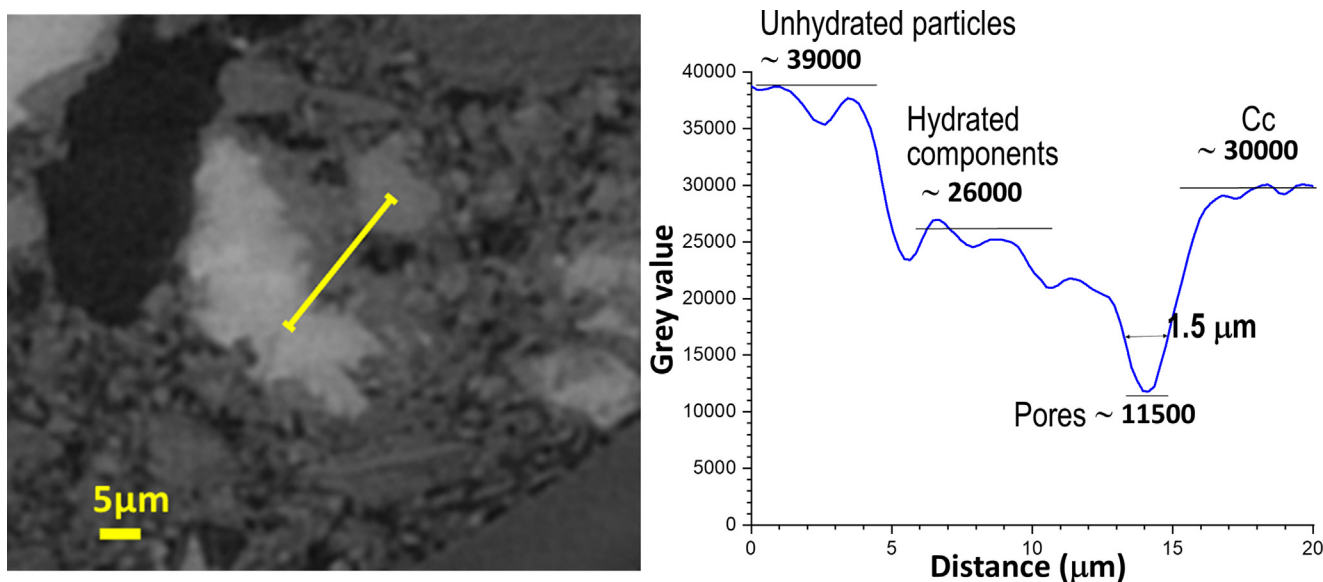

Fig. 10. (Left) Enlarged (selected) view reconstructed slice for PC-FC35-Cc-G-28d from Fig. 9c. (Right) Plot profile of the grey-scale values along the yellow line depicted in the left panel showing the presence of the four main components and highlighting that a narrow capillary pore of ~1.5 μm can be readily quantified. (For interpretation of the references to colour in this figure legend, the reader is referred to the web version of this article.)

To illustrate the high spatial resolution nature of the recorded synchrotron data, Fig. 10 displays an enlarged view of the highlighted region shown in Fig. 9c. The plot profile shown in Fig. 10-left allows us to visualize the four main components in the studied pastes: i) porosity (water and air) with grey-scale values ranging ~10000–16000; ii) hydrated components, ~16000–28000; iii) limestone, ~28000–33000; and iv) unhydrated cement particles, ~33000–45000. It can also be seen that a capillary pore, size ~1.5 μm, is readily measured which highlights the high resolution nature of the acquired data. It should be emphasised that although the voxel size was 0.325 μm the spatial resolution can be (much) poorer and here it is estimated to be ~1.0 μm.

4.8.1. Histogram analysis

A first (qualitative) data analysis can be done by inspecting the grey-scale histograms (GSHs). The linear attenuation coefficient μ is mapped in the reconstructed tomograms, where the higher is the μ value, the whiter is the corresponding grey-scale value. If the chemical stoichiometries and mass densities are known, the μ value can be calculated for the employed X-ray wavelength [50]. Stoichiometries and μ data for the phases present in LC³ bin-

ders are listed in Table 4 which help to understand the observed evolutions in the GSHs. Because of the non-unique nature of the inverse problem in obtaining the sectional images, the grey-scale values (or the linear attenuation coefficients) mapped onto the reconstructed 3D microstructure might not be the 'accurate' values of the corresponding components. Nevertheless, through a systematic data processing and analysis approach, the grey-scale values can provide useful insights on the features of the microstructures.

Fig. 11(a) shows the normalised GSHs for the Paganin reconstructions for the PC-FC35-Cc-G pastes cured with increasing hydration time. Additionally, and for the sake of comparison, this plot includes the profile for the neat PC paste cured during 7 days but with w/c = 0.50. As the images are reconstructed in 16-bits, the GSHs spans from 0 to 65,535 integer values. In order to illustrate the differences of contrast, Fig. 11(b) shows the corresponding normalised GSHs for the absorption reconstructions. However, it should be explicitly stated that the quantitative relationship between grey-scale values and the linear attenuation coefficients are lost in the Paganin reconstructions. Furthermore, placing the detector 5.5 mm far from the centre of the samples increases the contrast through the edge enhancement but it damages the direct

Table 4
Physical data for the main component phases in the studied cement pastes.

Component phase	Stoichiometry	Mass density/ gcm^{-3}	μ/ cm^{-1}
Water	H_2O	1.00	1.5
AS$_2$ (MK)	$Al_2Si_2O_7$	2.53	12.9
AFt	$Ca_6Al_2(SO_4)_3(OH)_{12} \cdot 26H_2O$	1.78	14.6
C$_2$ASH$_8$	$Ca_2Al_2SiO_7 \cdot 8H_2O$	1.94	16.0
Hc	$Ca_2Al(OH)_6[(CO_3)_{0.25}OH \cdot 5 2H_2O]$	1.90	20.0
C-S-H	$(CaO)_{1.8}(SiO_2)(H_2O)_4$	2.11$^\#$	23.7
CH	$Ca(OH)_2$	2.23	37.3
Cc	$CaCO_3$	2.71	34.5
C$_3$A	$Ca_3Al_2O_6$	3.05	46.5
C$_2$S	Ca_2SiO_4	3.30	52.7
C$_3$S	Ca_3SiO_5	3.15	54.7
C$_4$AF	Ca_2AlFeO_5	3.73	89.8

$^\#$ Mass density at the microscale for water saturated nanocrystalline C-S-H gel is taken from [51].

relationship between the grey-scale values and the linear attenuation coefficients.

Several observations can be drawn from the GSH displayed in Fig. 11(a). Firstly, the anhydrous component phases, the most absorbing phases see also Table 4, are located in the region 35000–55000 grey-scale and centred close to 42000. Secondly, the porosity (both water and air that cannot be resolved with the employed experimental setup) appears at grey-scale values between 8000 and 15000. Thirdly, the most abundant component is the set of hydrated phases which appears ~22000 grey-scale value. This set of voxels also includes, in addition to all the hydrated phases: i) any unreacted MK as its absorption is low, see Table 4; and ii) any water intermixed (embedded) within the hydrates below the spatial resolution of our measurements, ~1 µm, and hence, all gel water and a fraction of the capillary water is accounted for within this peak. It is noted that water/air have very low µ values, in comparison with the solid phases, and hence, the intermixing effect results in an increase of the amount of this component which is overall labelled as 'hydrated products'. Additionally, the width of this band narrows with the hydrating time reflecting the pore refinement below the spatial resolution as well as the paste homogenization with time due to the chemical reac-

tions which are taking place. Finally, and most important, the high spatial resolution and high contrast allow us to disentangle the calcite component. This phase is evident in the 28000–33000 grey-scale value interval as a minor peak. It must be mentioned that in the neat PC paste, which has a minor calcite content of ~2 wt %, this component is not visible.

4.8.2. Segmentation study

The three Paganin tomograms were segmented by manual thresholding using Dragonfly. The threshold selection was informed by the GSH shown in Fig. 11. Specifically, any voxel with a grey-scale value larger than 33,000 was labelled as unhydrated cement product (UHP). Voxels with grey-scale values lower than 16,000 were labelled as pores. The segmentation of calcite is not straightforward as the choice of the threshold between the hydrated products (HP) and calcite can play a significant role in the final output. Therefore, a preliminary study was carried out to determine the implications of this choice in the overall quantification. Fig. 12 shows the results of varying the HP/Cc threshold, from 27,500 to 29000, for the PC-FC35-Cc-G-28d tomogram. As expected for an overlapped histogram, by decreasing the value, the segmented amount of calcium carbonate increased. The obtained results were 5.2, 6.1, 7.2, and 8.4 vol% for the thresholds 29000, 28500, 28000, and 27500, respectively. A choice of a small threshold, 27500, not only resulted in a large fraction of calcium carbonate but other voxels of high grey-scale values, surrounding UHP, were labelled as Cc, see as an example the UHP particle highlighted with a white circle in Fig. 12. Conversely, the choice of a high threshold, 29000, led to the segmentation of a low fraction of calcium carbonate with particles being only partly accounted for. We consider this observation as very interesting as the smooth variation of the calcite particle segmentation indicates small regions of lower density within the calcite particles. To emphasise this, a raw picture of the highlighted calcite particle is also shown in the centre of Fig. 12. It is noted that this not only takes place in the surfaces of the CaCO$_3$ particles but also within the bulk of the particles suggesting that its dissolution/reaction takes place along the defects of such particles. This finding is in full agreement with the reactivity of limestone demonstrated in the thermal study. It was concluded that 28,500 grey-scale value was a reasonable compromise but it is explicitly acknowledged that this choice slightly
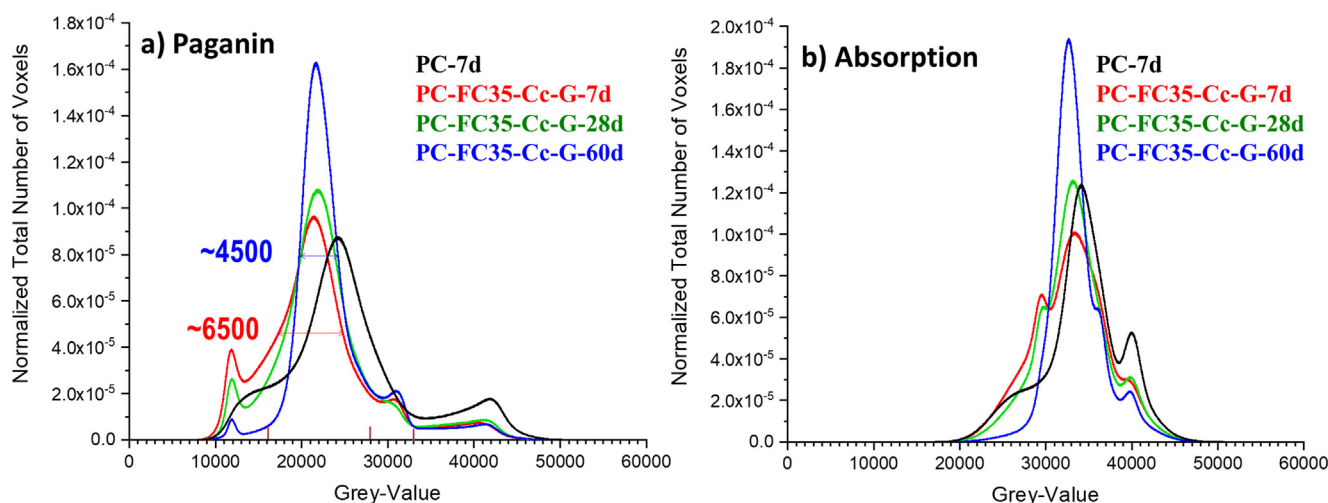

Fig. 11. Volume of interest normalised grey-scale histograms for PC-FC35-Cc-G pastes cured for 7, 28, and 60 days, (a) Paganin data, and (b) absorption data. The corresponding histogram for the neat PC pastes hydrated for 7 days is also given from reference [52]. The thick brown lines situated at 16000, 28500, and 33,000 grey-scale values are the thresholds used for data segmentation in the Paganin tomograms. The narrowing of the histogram for the hydrated component with the curing time is also highlighted.
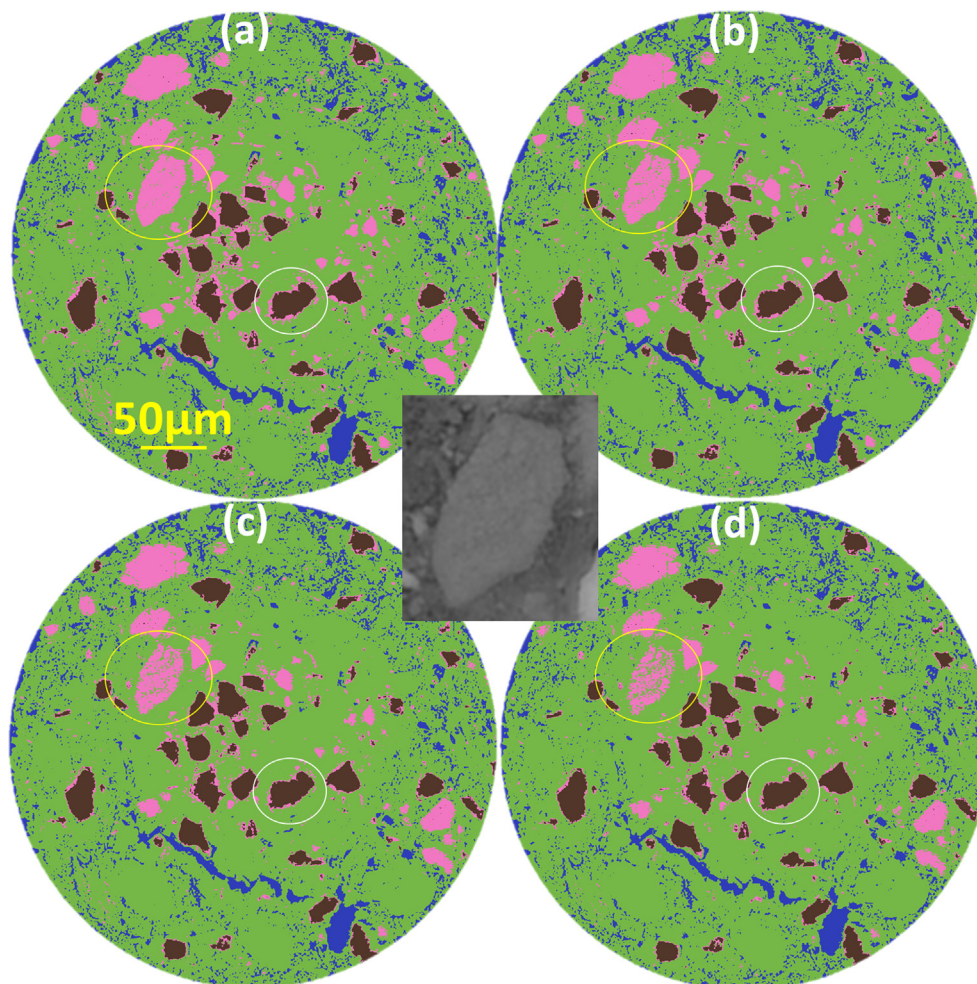
Fig. 12. Selected views of the segmentation outputs for the same tomogram, PC–FC35-Cc-G at 28 days, using variable threshold values. Pores (blue): grey-scale values always lower than 16000; UHP (brown): values always larger than 33000; HP (green); Calcite (pink). The threshold between HP and calcite was variable being 27500, 28000, 28500, and 29000, for panels (a), (b), (c) and (d) respectively. The segmented calcite particle highlighted with a yellow circle, its raw picture is also shown in the centre of the figure, strongly depends upon the threshold choice which reflects low X-ray absorbing zones due to partial dissolution. (For interpretation of the references to colour in this figure legend, the reader is referred to the web version of this article.)

affects the accuracy of the results of the segmentation. Furthermore, it is also noted that that the non-unique nature of the inverse problem in obtaining the reconstructed images could result in inaccuracies contributing to the observed features. However, by using the same data collection strategy and data processing protocols, this contribution is considered to be similar along the studied series. Fig. S10 shows selected orthoslices for the three tomograms highlighting the evolution of the calcite particles with time, noting that the segmentations were carried out using exactly the same thresholds.

Once, all the thresholds have been established, segmentation was carried out by labelling every voxel with the prescribed component depending upon the value of the grey-scale. The results are graphically displayed in Fig. 13 and the quantifications are reported in Table 5. Fig. 13 clearly shows that pore refinement is taken place with hydration time, and that the paste at 60 days is very densified with little remaining porosity at the length scale that can be accessed, 1 μm or larger. The quantified values of porosity, see Table 5, are difficult to discuss as it includes both water and air contributions. The sample preparation (capillary filling by the fresh paste) for this novel technique is still not optimised and it is not possible to ensure similar air contents in all

capillaries. It must be noted that the same capillary is not followed with time (that can be done at laboratory setups albeit with lower resolution and contrast), but here three different capillaries were filled at different times as the synchrotron experiment took place in one day. In order to eliminate this possible bias, the HP, Cc and UHP contents were recalculated leaving out the porosities. These values are also given in Table 5. Overall, UHP content decreases and the HP amount increases with hydration time, as expected. However, the variability due to the experimental procedures (filling of capillaries at different times) and the errors associated with the tomographic data analysis do not permit do accurately follow the calcite reaction. More robust procedures both for capillary filling (avoiding any possible microbleeding) and data analysis (segmentation beyond thresholding) are required to accurately follow the calcite content. In any case, the segmented values are reasonable as 28 days, the thermal analysis study and the RQPA work gave 10.2 and 11.6 wt% for limestone, respectively. The average transformed to vol% with the densities given in Table 4 resulted in 7.8 vol%. This value is close to the numbers given in Table 5, ~7.5 vol% indicating that the segmentation values are reasonable and that only minor adjustments are needed to fully capture the calcite evolution in these systems. It would be preferred to
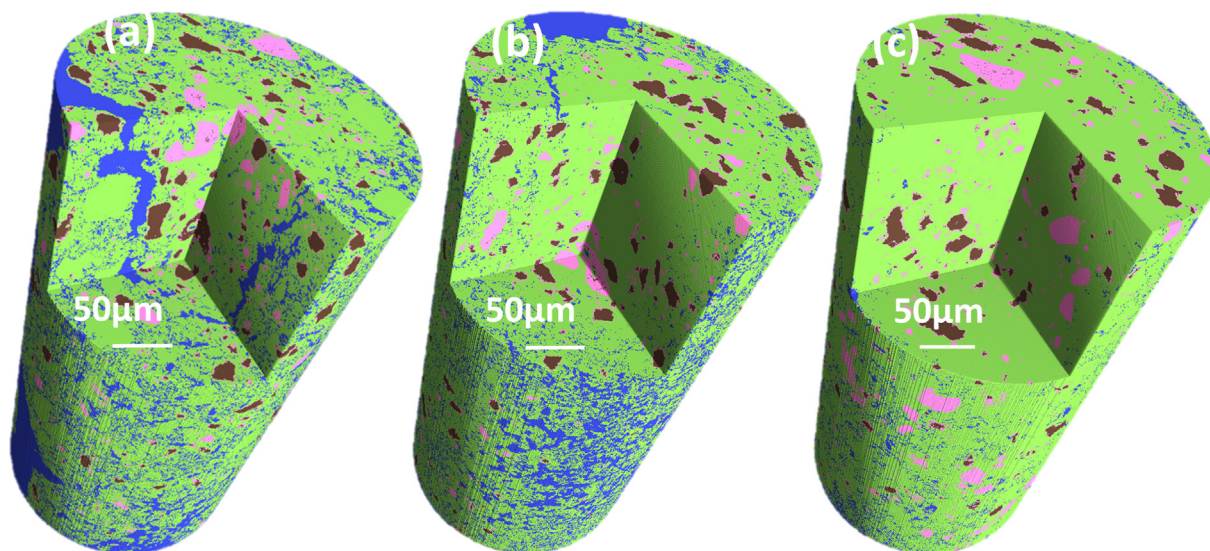
Fig. 13. Rendered volumes of the final segmentations for the LC^3 binder with 50% cement replacement, PC-FC35-Cc-G, at 7, 28, and 60 days of hydration for panels (a), (b) and (c), respectively. Unhydrated cement components (brown), limestone (pink), hydrated products (green), and water and air porosities (blue). Voxel size = 0.325 µm. Estimated spatial resolution: ~1 µm. (For interpretation of the references to colour in this figure legend, the reader is referred to the web version of this article.)

Table 5
Segmentation results of the synchrotron microtomographies for PC-FC35-Cc-G pastes by using the thresholds given in the caption of Fig. 11.

Sample	Pores (vol%)	HP (vol%)	Cc (vol%)	UHP (vol%)	rHP[#] (vol%)	rCc[#] (vol%)	rUHP[#] (vol%)
PC-FC35-Cc-G-7d	16.6	70.4	6.5	6.5	84.4	7.8	7.8
PC-FC35-Cc-G-28d	10.0	76.3	6.1	7.6	84.8	6.8	8.4
PC-FC35-Cc-G-60d	2.4	84.0	7.6	6.0	86.0	7.8	6.2

[#] rHP, rCc and rUHP stand for the renormalized values of these components without porosities.

follow the same capillary with hydration time but that tradeoff would forego the required high spatial resolution and sufficient contrast to distinguish limestone from the hydrated products. Laboratory microtomography, which has a much easier access, is unlikely to meet these stringent requirements, at least with currently available instrumentation if phase-contrast procedures are not implemented.

To finish the porosity discussion, it should be noted the two largest sources of inaccuracies. On the one hand, there are image processing variability during the reconstruction and data analysis steps. Here, parallel monochromatic synchrotron radiation helps in minimizing the most common sources of errors [53,54]. On the other hand, there are experimental issues that still remain be solved for the building materials field. As indicated above, one of the most important problem is the inefficient filling of the narrow capillaries needed to access to high resolution. In some cases, large voids with dimensions bigger than 50 µm are observed. Furthermore, for some capillaries, air porosity is concentrated close to the glass capillary walls. More research is needed to produce capillaries densely filled with pastes in order to follow the water porosities which should not be masked by the entrapped air due to poor filling.

4.8.3. Pore connectivity study
Pore connectivity analysis was carried out with Dragonfly to differentiate pores that are connected to the surface of the evaluated sample volume from those pores that are isolated. After labeling the surface pixels, connected components analysis was used to sort all pore pixels into those that connect to the surface from those that are disconnected. Connectivity stringency criteria of whether to consider two voxels as connected can be varied to either include or exclude voxels that connect on the voxel-face (6-connectivtiy) or connect on the corners (26-connectivity). Details about data processing related to connectivity analysis are given in standard texts [55]. Obviously, connectivity fraction labeled as connected increases under that the corner-connectivity criterion. This processing was carried out for the three tomograms, for both 6- and 26-connected porosity, by defining a top and bottom planes perpendicular to the capillary length. Out of the total pore volume given in Table 5, 92, 78 and 9% were found linked by the 6-connected porosity for PC-FC35-Cc-G-7d, PC-FC35-Cc-G-28d and PC-FC35-Cc-G-60d, respectively. It is emphasized that this last sample, not only have very low total porosity, 2.4 vol%, but its connectivity as defined above is quite low 9%. These results are graphically shown in Fig. 14 where both total porosity and the 6-connected porosity are shown in binarized images. By applying the 26-connected porosity operation, 93, 83 and 16% were found linked at 7, 28 and 60 days of hydration, respectively. The decrease in pore connectivities measured for these LC^3 samples, with the two (related) approaches, has important consequences for the permeabilities to different chemical species. Lower connectivities will likely yield lower permeabilities. However, studies directly relating the X-ray tomographycally-determined connectivities and durability performances are still to be developed.
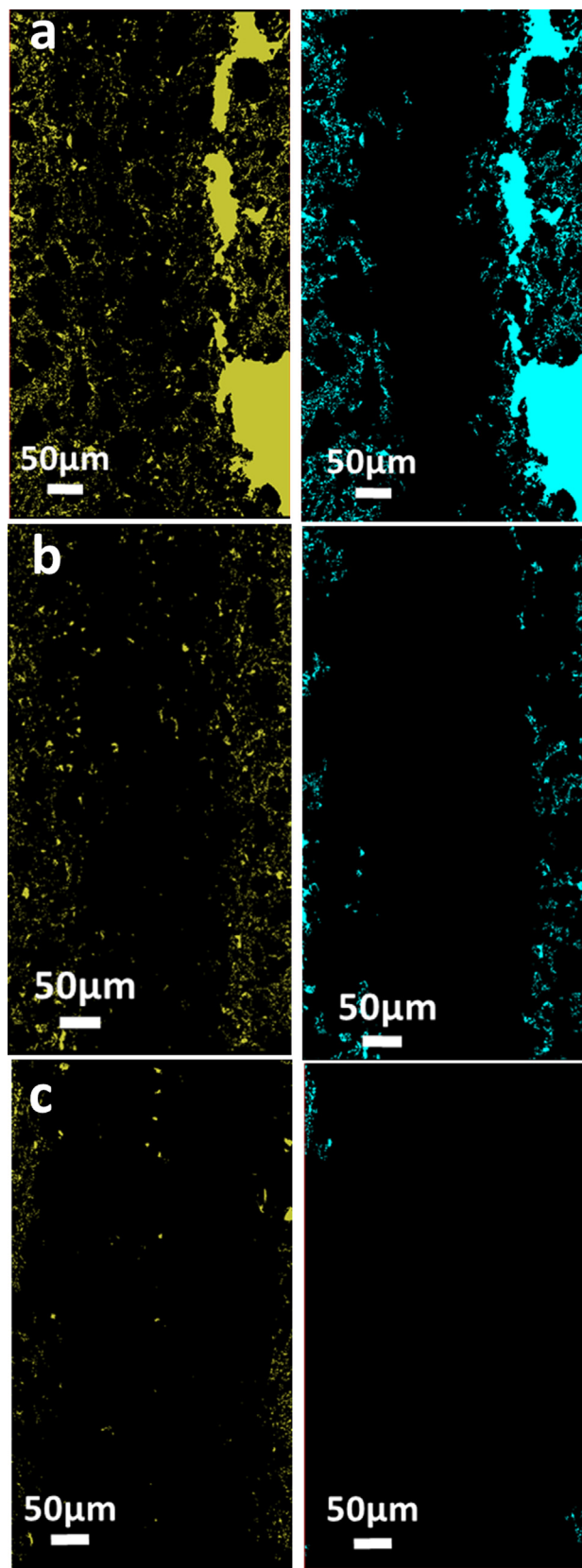
5. Conclusions

This work has studied a limestone calcined clay binder with 48 wt% replacement of the Portland cement by: i) 30 wt% of a calcined clay with an original kaolinite content of ~75 wt%; ii) 15 wt% of limestone; and iii) 3 wt% of gypsum. The employed cement had 3 wt% of calcium sulphates and 4 wt% of calcite, and hence the studied binder has a clinker factor replacement slightly larger than 50%. Even so, the mortar prepared (w/b = 0.40) had 43 MPa at 7 days of hydration, higher than that of the reference neat Portland mortar, 34 MPa (w/c = 0.50). The enhanced mechanical properties are maintained at 28 days. The phase development has been followed by Rietveld quantitative phase analysis, thermal analysis, and ^{27}Al MAS-NMR. Chiefly, thermal analysis has established a decrease of the calcite content with hydration time due to its reactivity. The only carbonate-containing crystalline phase measured by powder diffraction was AFm-type hemicarbonate. This does not preclude the existence of other carbonate-containing amorphous phase(s). Further investigations are planned to clarify this issue.

The microstructures of the resulting pastes, and their time evolution, have been studied by mercury intrusion porosimetry and synchrotron X-ray microtomography. MIP reveals a pore refinement of the PC-FC35-Cc-G from 7 to 28 days of hydration in agreement with the phase development revealed by powder diffraction and the calcite reactivity shown by thermal analysis. Above all, high-resolution synchrotron microtomography with phase-contrast has allowed following four components: i) water and air porosities; ii) hydrated products; iii) calcite; and iv) unhydrated products. On the one hand, the high-resolution high-contrast data allowed distinguishing between closely-absorbing phases: calcite and the hydration products. Furthermore, clear signatures of calcite particle reactivity were evident in the tomograms at later hydration ages. On the other hand, the porosity has been segmented within our resolution (0.325 μm of voxel size, ~1 μm of estimated 3D spatial resolution) and pore refinement has been clearly measured. Furthermore, it has also been established a pronounced drop of pore connectivities between 28 and 60 days of hydration. The decrease in pore connectivities measured for these samples has important consequences for the permeability to different chemical species including chlorides. A next step in our investigations is to carry out similar studies with high resolution laboratory microtomography to try to establish the decrease in pore connectives with time in the same samples within the same capillaries.

6. Data availability

The synchrotron tomography raw data corresponding to this work are available from the authors upon request. In addition, LXRPD, Thermal analysis, MIP, calorimetry, PSD, ^{27}Al MAS-NMR raw data can be freely accessed on Zenodo at https://doi.org/10.5281/zenodo.4473084, and used under the Creative Commons Attribution license. More details are given in Supplementary Information.

CRediT authorship contribution statement

Isabel M.R. Bernal: Investigation, Methodology, Data curation, Writing - review & editing. **Shiva Shirani:** Investigation, Data curation, Writing - review & editing. **Ana Cuesta:** Investigation, Methodology, Funding acquisition, Writing - review & editing. **Isabel Santacruz:** Investigation, Writing - review & editing. **Miguel A. G. Aranda:** Conceptualization, Supervision, Writing - review & editing.

Fig. 14. Selected axial slices of the tomograms for PC-FC35-Cc-G after binarizing the data and showing the overall porosity (yellow) in the left panels, and the 6-connected porosity (light blue) in the right panels. Hydration times are (a) 7 days, (b) 28 days, and (c) 60 days. (For interpretation of the references to colour in this figure legend, the reader is referred to the web version of this article.)

Declaration of Competing Interest

The authors declare that they have no known competing financial interests or personal relationships that could have appeared to influence the work reported in this paper.

Acknowledgements

Appendix A. Supplementary data

Supplementary data to this article can be found online at https://doi.org/10.1016/j.conbuildmat.2021.124054.

References

[1] L. Barcelo, J. Kline, G. Walenta, E. Gartner, Cement and carbon emissions, Mater. Struct. 47 (6) (2014) 1055–1065, https://doi.org/10.1617/s11527-013-0114-5.

[2] I. Amato, Green cement: Concrete solutions, Nature. 494 (7437) (2013) 300–301, https://doi.org/10.1038/494300a.

[3] U.N. Environment, K.L. Scrivener, V.M. John, E. Gartner, Eco-efficient cements: Potential, economically viable solutions for a low-CO2, cement-based materials industry, Cem. Concr. Res. 114 (2018) 2–26, https://doi.org/10.1016/j.cemconres.2018.03.015.

[4] C. Shi, B. Qu, J.L. Provis, Recent progress in low-carbon binders, Cem. Concr. Res. 122 (2019) 227–250, https://doi.org/10.1016/J.CEMCONRES.2019.05.009.

[5] M.C.G. Juenger, R. Snellings, S.A. Bernal, Supplementary cementitious materials: New sources, characterization, and performance insights, Cem. Concr. Res. 122 (2019) 257–273, https://doi.org/10.1016/J.CEMCONRES.2019.05.008.

[6] M.C.G. Juenger, R. Siddique, Recent advances in understanding the role of supplementary cementitious materials in concrete, Cem. Concr. Res. 78 (2015) 71–80, https://doi.org/10.1016/j.cemconres.2015.03.018.

[7] B. Lothenbach, K. Scrivener, R.D. Hooton, Supplementary cementitious materials, Cem. Concr. Res. 41 (12) (2011) 1244–1256, https://doi.org/10.1016/j.cemconres.2010.12.001.

[8] J. Skibsted, R. Snellings, Reactivity of supplementary cementitious materials (SCMs) in cement blends, Cem. Concr. Res. 124 (2019) 105799, https://doi.org/10.1016/j.cemconres.2019.105799.

[9] V.M. John, B.L. Damineli, M. Quattrone, R.G. Pileggi, Fillers in cementitious materials — Experience, recent advances and future potential, Cem. Concr. Res. 114 (2018) 65–78, https://doi.org/10.1016/J.CEMCONRES.2017.09.013.

[10] K.L. Scrivener, F. Martirena, S. Bishnoi, S. Maity, Calcined clay limestone cements (LC3), Cem. Concr. Res. 114 (2018) 49–56, https://doi.org/10.1016/j.cemconres.2017.08.017.

[11] K. Scrivener, F. Avet, H. Maraghechi, F. Zunino, J. Ston, W. Hanpongpun, A. Favier, Impacting factors and properties of limestone calcined clay cements (LC3), Green Mater. 7 (1) (2019) 3–14, https://doi.org/10.1680/jgrma.18.00029.

[12] F. Zunino, K. Scrivener, The reaction between metakaolin and limestone and its effect in porosity refinement and mechanical properties, Cem. Concr. Res. 140 (2021) 106307, https://doi.org/10.1016/j.cemconres.2020.106307.

[13] B. Fabbri, S. Gualtieri, C. Leonardi, Modifications induced by the thermal treatment of kaolin and determination of reactivity of metakaolin, Appl. Clay Sci. 73 (2013) 2–10, https://doi.org/10.1016/j.clay.2012.09.019.

[14] A. Tironi, M.A. Trezza, A.N. Scian, E.F. Irassar, Potential use of Argentine kaolinitic clays as pozzolanic material, Appl. Clay Sci. 101 (2014) 468–476, https://doi.org/10.1016/j.clay.2014.09.009.

[15] S.C. Taylor-Lange, E.L. Lamon, K.A. Riding, M.C.G. Juenger, Calcined kaolinite-bentonite clay blends as supplementary cementitious materials, Appl. Clay Sci. 108 (2015) 84–93, https://doi.org/10.1016/j.clay.2015.01.025.

[16] T. Danner, G. Norden, H. Justnes, Characterisation of calcined raw clays suitable as supplementary cementitious materials, Appl. Clay Sci. 162 (2018) 391–402, https://doi.org/10.1016/j.clay.2018.06.030.

[17] A. Tironi, F. Cravero, A.N. Scian, E.F. Irassar, Pozzolanic activity of calcined halloysite-rich kaolinitic clays, Appl. Clay Sci. 147 (2017) 11–18, https://doi.org/10.1016/j.clay.2017.07.018.

[18] A. Alujas, R. Fernández, R. Quintana, K.L. Scrivener, F. Martirena, Pozzolanic reactivity of low grade kaolinitic clays: Influence of calcination temperature and impact of calcination products on OPC hydration, Appl. Clay Sci. 108 (2015) 94–101, https://doi.org/10.1016/j.clay.2015.01.028.

[19] Y. Cao, Y. Wang, Z. Zhang, Y. Ma, H. Wang, Recent progress of utilization of activated kaolinitic clay in cementitious construction materials, Compos. Part B. 211 (2021) 108636, https://doi.org/10.1016/j.compositesb:2021.108636.

[20] F. Avet, K. Scrivener, Influence of pH on the chloride binding capacity of Limestone Calcined Clay Cements (LC3), Cem. Concr. Res. 131 (2020) 106031, https://doi.org/10.1016/j.cemconres.2020.106031.

[21] Z. Shi, M.R. Geiker, K. De Weerdt, T.A. Østnor, B. Lothenbach, F. Winnefeld, J. Skibsted, Role of calcium on chloride binding in hydrated Portland cement–metakaolin–limestone blends, Cem. Concr. Res. 95 (2017) 205–216, https://doi.org/10.1016/j.cemconres.2017.02.003.

[22] H. Maraghechi, F. Avet, H. Wong, H. Kamyab, K.L. Scrivener, Performance of Limestone Calcined Clay Cement (LC3) with various kaolinite contents with respect to chloride transport, Mater. Struct. 51 (2018) 125, https://doi.org/10.1617/s11527-018-1255-3.

[23] S. Sui, W. Wilson, F. Georget, H. Maraghechi, H. Kazemi-Kamyab, W. Sun, K. Scrivener, Quantification methods for chloride binding in Portland cement and limestone systems, Cem. Concr. Res. 125 (2019) 105864, https://doi.org/10.1016/j.cemconres.2019.105864.

[24] M. Gbozee, K. Zheng, F. He, X. Zeng, The influence of aluminum from metakaolin on chemical binding of chloride ions in hydrated cement pastes, Appl. Clay Sci. 158 (2018) 186–194, https://doi.org/10.1016/j.clay.2018.03.038.

[25] R. Siddique, J. Klaus, Influence of metakaolin on the properties of mortar and concrete: A review, Appl. Clay Sci. 43 (3-4) (2009) 392–400, https://doi.org/10.1016/j.clay.2008.11.007.

[26] B.B. Sabir, S. Wild, J. Bai, Metakaolin and calcined clays as pozzolans for concrete: A review, Cem. Concr. Compos. 23 (6) (2001) 441–454, https://doi.org/10.1016/S0958-9465(00)00092-5.

[27] R.S. Nicolas, M. Cyr, G. Escadeillas, Characteristics and applications of flash metakaolins, Appl. Clay Sci. 83–84 (2013) 253–262, https://doi.org/10.1016/j.clay.2013.08.036.

[28] M. Antoni, J. Rossen, F. Martirena, K. Scrivener, Cement substitution by a combination of metakaolin and limestone, Cem. Concr. Res. 42 (12) (2012) 1579–1589, https://doi.org/10.1016/j.cemconres.2012.09.006.

[29] D.P. Bentz, P.E. Stutzman, F. Zunino, Low-temperature curing strength enhancement in cement-based materials containing limestone powder, Mater. Struct. Constr. 50 (2017) 173, https://doi.org/10.1617/s11527-017-1042-6.

[30] Y. Dhandapani, M. Santhanam, Investigation on the microstructure-related characteristics to elucidate performance of composite cement with limestone-calcined clay combination, Cem. Concr. Res. 129 (2020) 105959, https://doi.org/10.1016/j.cemconres.2019.105959.

[31] G. Mishra, A.C. Emmanuel, S. Bishnoi, Influence of temperature on hydration and microstructure properties of limestone-calcined clay blended cement, Mater. Struct. Constr. 52 (2019) 91, https://doi.org/10.1617/s11527-019-1390-5.

[32] S. Brisard, M. Serdar, P.J.M. Monteiro, Multiscale X-ray tomography of cementitious materials: A review, Cem. Concr. Res. 128 (2020) 105824, https://doi.org/10.1016/j.cemconres.2019.105824.

[33] W. Kong, Y.a. Wei, S. Wang, J. Chen, Y. Wang, Research progress on cement-based materials by X-ray computed tomography, Int. J. Pavement Res. Technol. 13 (4) (2020) 366–375, https://doi.org/10.1007/s42947-020-0119-8.

[34] A. du Plessis, W.P. Boshoff, A review of X-ray computed tomography of concrete and asphalt construction materials, Constr. Build. Mater. 199 (2019) 637–651, https://doi.org/10.1016/j.conbuildmat.2018.12.049.

[35] A.C. Larson, R.B. Von Dreele, General structure analysis system (GSAS), Los Alamos Natl. Lab. Rep. LAUR. 748 (2004) 86–748.

[36] A.G. De La Torre, S. Bruque, M.A.G. Aranda, Rietveld quantitative amorphous content analysis, J. Appl. Crystallogr. 34 (2) (2001) 196–202, https://doi.org/10.1107/S0021889801002485.

[37] J.D. Zea-Garcia, A.G. De la Torre, M.A.G. Aranda, I. Santacruz, Processing and characterisation of standard and doped alite-belite-ye ' elimite ecocement pastes and mortars, Cem. Concr. Res. 127 (2020) 105911, https://doi.org/10.1016/j.cemconres.2019.105911.

[38] K.L. Scrivener, R. Snellings, B. Lothenbach, A Practical Guide to Microstructural Analysis of Cementitious Materials, CRC Press, Boca Raton, FL, 2016.

[39] D. Paganin, S.C. Mayo, T.E. Gureyev, P.R. Miller, S.W. Wilkins, Simultaneous phase and amplitude extraction from a single defocused image of a homogeneous object, J. Microsc. 206 (1) (2002) 33–40, https://doi.org/10.1046/j.1365-2818.2002.01010.x.

[40] F. Marone, M. Stampanoni, Regridding reconstruction algorithm for real-time tomographic imaging, J. Synchrotron Radiat. 19 (6) (2012) 1029–1037, https://doi.org/10.1107/S0909049512032864.

[41] F. Zunino, K. Scrivener, The influence of the filler effect on the sulfate requirement of blended cements, Cem. Concr. Res. 126 (2019) 105918, https://doi.org/10.1016/j.cemconres.2019.105918.

[42] M.A.G. Aranda, A.G. De La Torre, L. Leon-Reina, Rietveld Quantitative Phase Analysis of OPC Clinkers, Cements and Hydration Products, Rev. Mineral. Geochemistry. 74 (1) (2012) 169–209, https://doi.org/10.2138/rmg.2012.74.5.

[43] B. Lothenbach, P. Durdzinski, K. De Weerdt, Thermogravimetric analysis. In: B. L. K. Scrivener, R. Snellings (Ed.), A Pract. Guid. to Microstruct. Anal. Cem. Mater., CRC Press, U.S.A, 2016: pp. 177–211.

[44] J. Skibsted, E. Henderson, H.J. Jakobsen, Characterization of Calcium Aluminate Phases in Cements by 27Al MAS NMR Spectroscopy, Inorg. Chem. 32 (1993) 1013–1027, https://doi.org/10.1021/ic00058a043.

[45] M. Daugaard Andersen, H.J. Jakobsen, Jø. Skibsted, Incorporation of aluminum in the calcium silicate hydrate (C-S-H) of hydrated Portland cements: A high-

field 27Al and 29Si MAS NMR investigation. Inorg. Chem. 42 (2003) 2280–2287. https://doi.org/10.1021/ic020607b.

[46] Z. Dai, T.T. Tran, J. Skibsted, Aluminum Incorporation in the C-S-H Phase of White Portland Cement-Metakaolin Blends Studied by [27] Al and [29] Si MAS NMR Spectroscopy, J. Am. Ceram. Soc. 97 (8) (2014) 2662–2671, https://doi.org/10.1111/jace:13006.

[47] Aslam Kunhi Mohamed, Pinelopi Moutzouri, Pierrick Berruyer, Brennan J. Walder, Jirawan Siramanont, Maya Harris, Mattia Negroni, Sandra C. Galmarini, Stephen C. Parker, Karen L. Scrivener, Lyndon Emsley, Paul Bowen, The Atomic-Level Structure of Cementitious Calcium Aluminate Silicate Hydrate, J. Am. Chem. Soc. 142 (25) (2020) 11060–11071, https://doi.org/10.1021/jacs.0c0298810.1021/jacs.0c02988.s00110.1021/jacs.0c02988.s002.

[48] I. Santacruz, Á.G. De la Torre, G. Álvarez-Pinazo, A. Cabeza, A. Cuesta, J. Sanz, M.A.G Aranda, Structure of stratlingite and effect of hydration methodology on microstructure, Adv. Cem. Res. 28 (1) (2016) 13–22, https://doi.org/10.1680/adcr.14.00104.

[49] G. Cardinaud, E. Rozière, O. Martinage, A. Loukili, L. Barnes-Davin, M. Paris, D. Deneele, Calcined clay – Limestone cements: Hydration processes with high and low-grade kaolinite clays, Constr. Build. Mater. 277 (2021) 122271, https://doi.org/10.1016/j.conbuildmat.2021.122271.

[50] B.L. Henke, E.M. Gullikson, J.C. Davis, X-Ray Interactions: Photoabsorption, Scattering, Transmission, and Reflection at E = 50–30,000 eV, Z = 1–92, At. Data Nucl. Data Tables. 54 (1993) 181–342.

[51] A. Cuesta, Á.G. De la Torre, I. Santacruz, A. Diaz, P. Trtik, M. Holler, B. Lothenbach, M.A.G. Aranda, Quantitative disentanglement of nanocrystalline phases in cement pastes by synchrotron ptychographic X-ray tomography, IUCrJ. 6 (3) (2019) 473–491, https://doi.org/10.1107/S205225251900377410.1107/S2052252519003774/ro5017sup1.pdf.

[52] S. Shirani, A. Cuesta, A. Morales-Cantero, A.G. De la Torre, M.P. Olbinado, M.A.G. Aranda, Influence of curing temperature on belite cement hydration: A comparative study with Portland cement, Cem. Concr. Res. 147 (2021) 106499, https://doi.org/10.1016/j.cemconres.2021.106499.

[53] E. Maire, P.J. Withers, Quantitative X-ray tomography, Int. Mater. Rev. 59 (1) (2014) 1–43, https://doi.org/10.1179/1743280413Y.0000000023.

[54] Y. Obata, H.A. Bale, H.S. Barnard, D.Y. Parkinson, T. Alliston, C. Acevedo, Quantitative and qualitative bone imaging: A review of synchrotron radiation microtomography analysis in bone research, J. Mech. Behav. Biomed. Mater. 110 (2020) 103887, https://doi.org/10.1016/j.jmbbm.2020.103887.

[55] J. Ohser, K. Schladitz. Chapter 4. Image Processing, in: 3D Images Mater. Struct. Process. Anal. WILEY-VCH, Weinheim. 2009. 79–148. https://doi.org/10.1002/9783527628308.

Phase and microstructure evolutions in LC³ binders by multi-technique approach including synchrotron microtomography

Isabel M. R. Bernal, Shiva Shirani, Ana Cuesta, Isabel Santacruz, Miguel A. G. Aranda*

¹Departamento de Química Inorgánica, Cristalografía y Mineralogía, Universidad de Málaga, Málaga, 29071, Spain.

* email: g_aranda@uma.es

This PDF file includes:

→ **Raw data availability and description.**

→ **#10 supplementary Figures:**

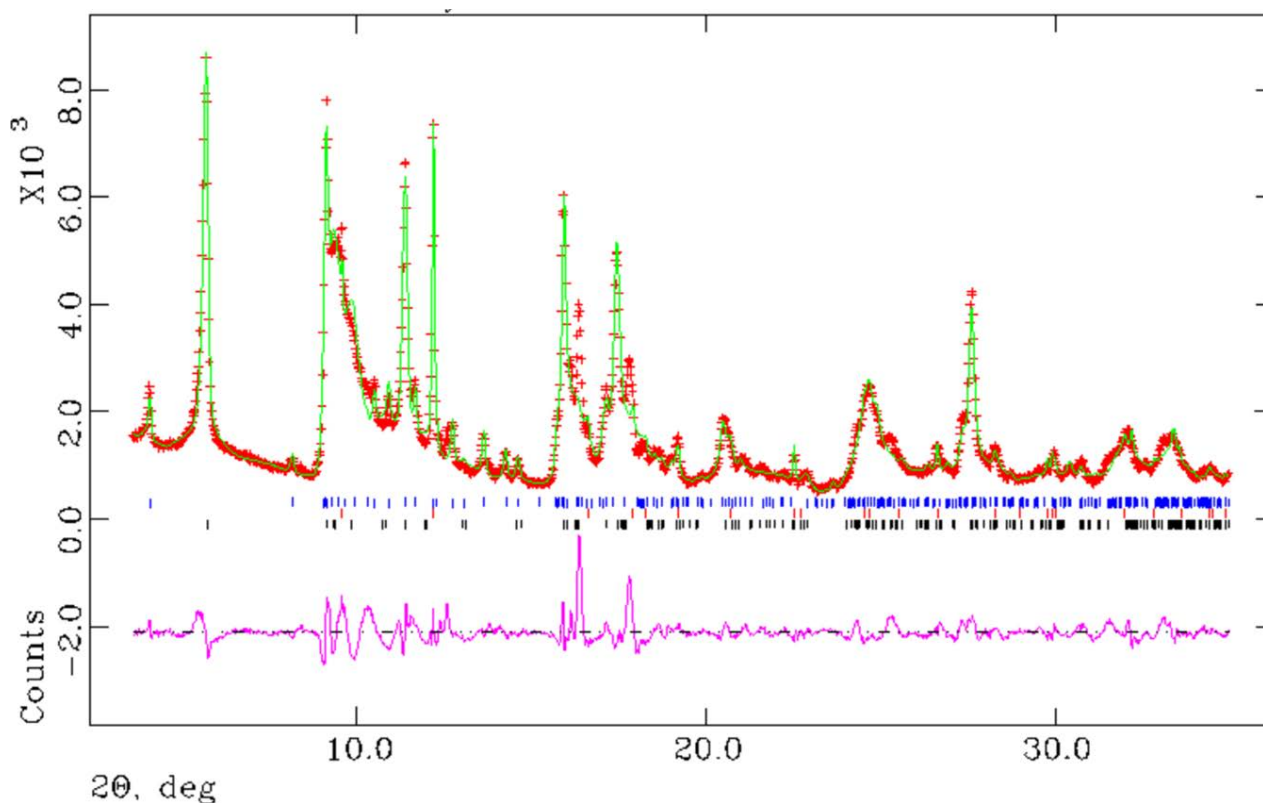**Figure S1.** Rietveld plot, Mo-Kα_1 strictly monochromatic radiation (λ=0.71 Å), for the raw FC35 clay resulting in a phase composition: kaolinite: 85 wt%, quartz: 3 wt%, and muscovite 12 wt%. Some additional diffraction peaks were not accounted for, and hence the kaolinite content is likely slightly lower.

Figure S2. Thermal analysis traces (green – weight loss; blue – derivative of the weight loss; and brown – heat flow) for the raw FC35 clay showing the weight loss in the key kaolinite range. From this loss (400-700ºC temperature range), a kaolinite content of 72.5 wt% is derived.

Figure S3. Laboratory X-ray powder diffraction pattern, Cu Kα_1 radiation, (λ=1.54 Å), for the FC35 clay calcined at 860 ºC in a brick-fabrication industrial oven. The sample contains muscovite and quartz. Kaolinite is no longer present and metakaolin is evident as a scattering bump centered at 25 ° (2Θ).

Figure S4. Heat flow traces for PC-FC35-Cc system with increasing amounts of additional gypsum. From the curves, it is inferred that 3 wt% gypsum additional dosage is suitable to have the second calorimetry peak (C₃A-due) well after the first (alite-due) peak.

Figure S5. Rietveld plots, Mo-Kα_1 strictly monochromatic radiation (λ=0.71 Å), for the PC-FC35-Cc-G pastes at the indicated hydration ages. The patterns also contain the quartz diffraction peaks, used as an internal standard to determine the overall amount of amorphous phase.

Figure S6. Rietveld plots, Mo-Kα_1 strictly monochromatic radiation (λ=0.71 Å), for the PC-MK-G pastes at the indicated hydration ages. The patterns also contain the quartz diffraction peaks, used as an internal standard to determine the overall amount of amorphous phase.

Figure S7. Thermal analysis traces (green – weight loss; blue – derivative of the weight loss; and brown – heat flow) for the PC-FC35-Cc-G pastes at the studied hydration ages: (a) 2 days, (b) 7 days, (c) 28 days and (d) 60 days.

Figure S8. Thermal analysis traces (green – weight loss; blue – derivative of the weight loss; and brown – heat flow) for the PC-MK-G pastes at the studied hydration ages: (a) 2 days, (b) 7 days and (c) 28 days.

Figure S9. Selected BSE-SEM microphotograph for PC-FC35-Cc-G paste after 28 days of hydration.

Figure S10. Top row: selected views of the Paganin reconstructed orthoslices for: (a) PC-FC35-Cc-G-7d, (b) PC-FC35-Cc-G-2d and (c) PC-FC35-Cc-G-60d. Calcite particles are highlited in red. Bottom row: segmentation outputs for the regions highlighted with a yellow squares. Pores (blue, gsv≤16,000), HP (green, 16,000<gsv≤28,500), Calcite (pink, 28,500<gsv≤33,000), and UHP (brown, 33,000<gsv); gsv=grey scale value.

● Raw data availability and description

Tomographic reconstructed raw data (6 tomograms) are available from the authors upon request. Interested researchers in the synchrotron tomographic reconstructed data should be aware of the size of these files which are given in the following table. A hard drive could be necessary.

File Name	Zipped File Size* (by 7Zip app.)	Additional information
33_PC-FC35-Cc-G-7d (Paganin)	21.8Gb	
33_PC-FC35-Cc-G-7d (Absorption)	21.8Gb	
15_PC-FC35-Cc-G-28d (Paganin)	21.6Gb	PC-FC35-Cc-G-Hydration Age
15_PC-FC35-Cc-G-28d (Absorption)	21.5Gb	
30_PC-FC35-Cc-G-60d (Paganin)	21.6Gb	
30_PC-FC35-Cc-G-60d (Absorption)	21.5Gb	
Total size of all datasets :	**129.8Gb**	

Original file size for every single dataset is 27.4GB

Additionally, the raw data for calorimetry, MIP, LXRPD, NMR and PSD are uploaded on Zenodo in text file or excel format. The thermal analysis files are also on Zenodo and can be open using the TA Universal Analysis software. Data can be accessed at: https://doi.org/10.5281/zenodo.4473084.

● Figures

Figure S1. Rietveld plot, Mo-Kα_1 strictly monochromatic radiation (λ=0.71 Å), for the raw FC35 clay resulting in a phase composition: kaolinite: 85 wt%, quartz: 3 wt%, and muscovite 12 wt%. Some additional diffraction peaks were not accounted for, and hence the kaolinite content is likely (slightly) lower.
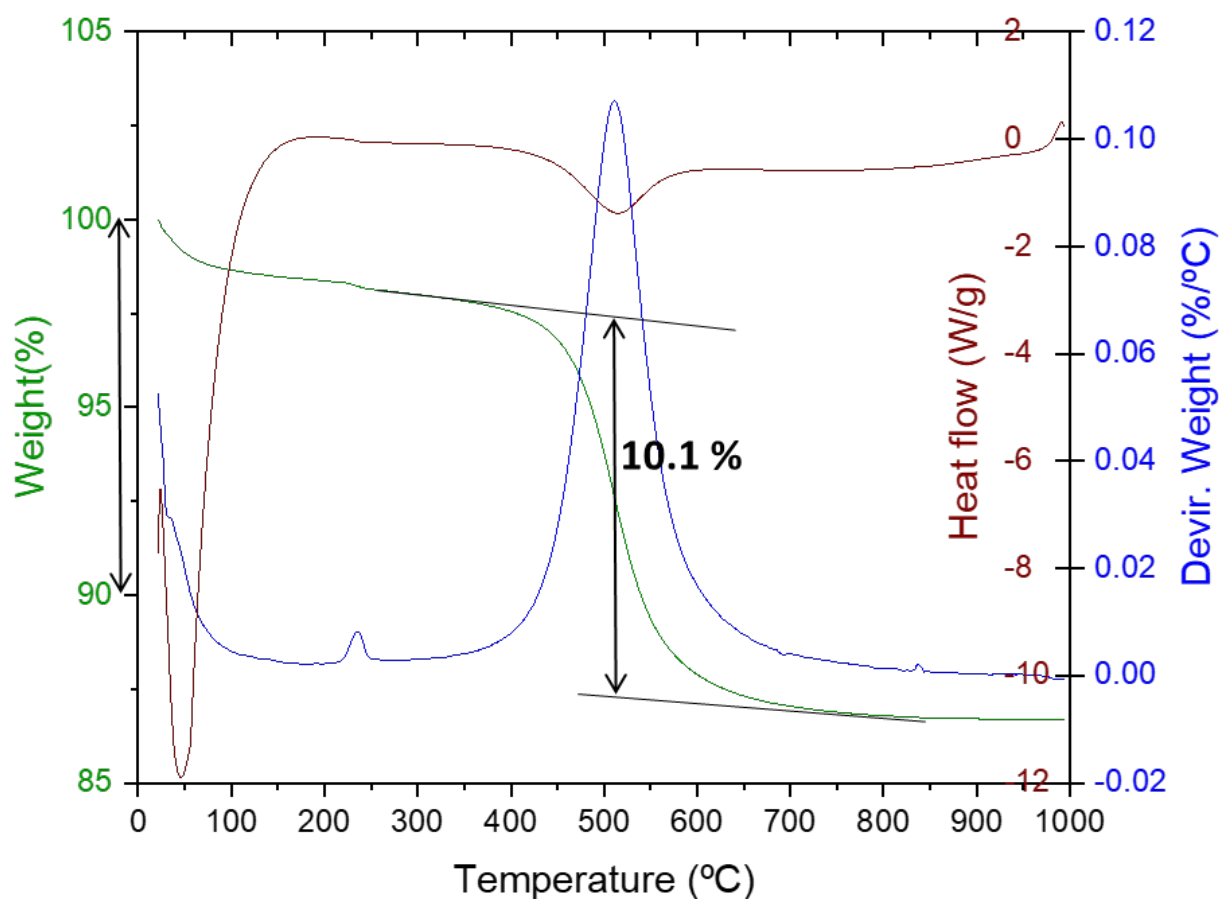
Figure S2. Thermal analysis traces (green – weight loss; blue – derivative of the weight loss; and brown – heat flow) for the raw FC35 clay showing the weight loss in the key kaolinite range. From this loss (400-700ºC temperature range), a kaolinite content of 72.5 wt% is derived.
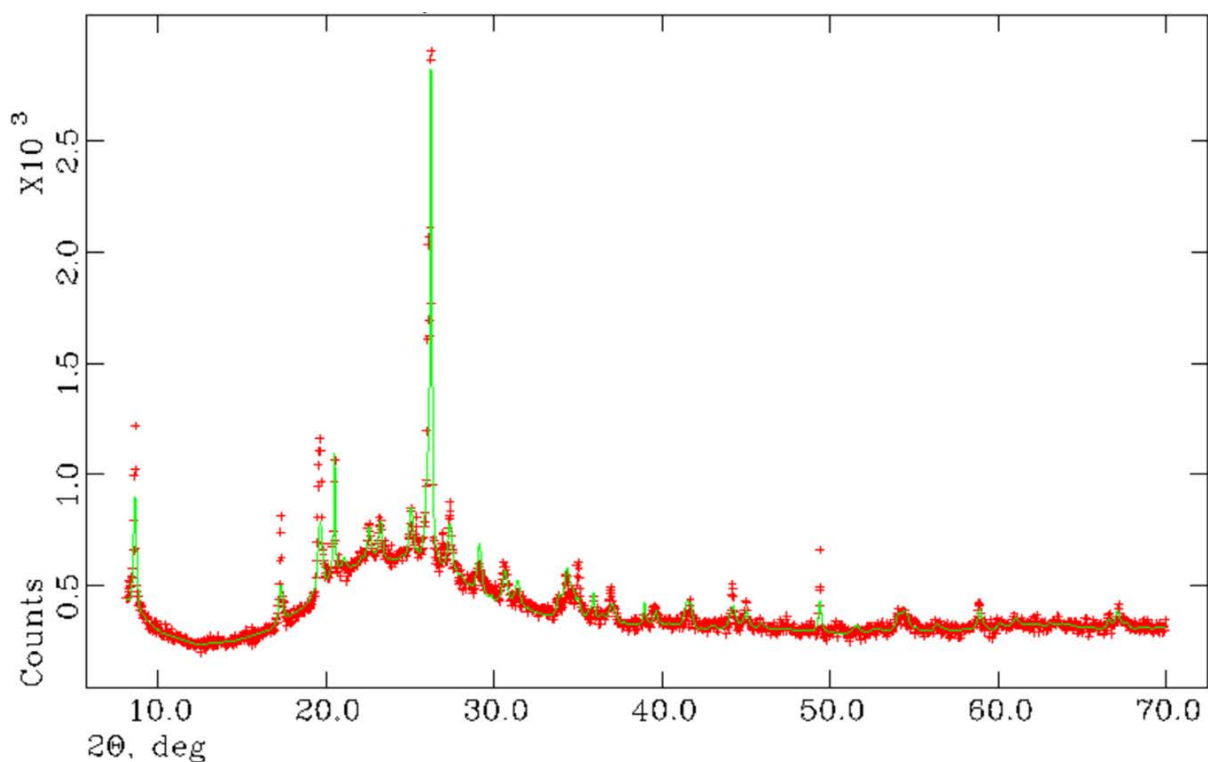

Figure S3. Laboratory X-ray powder diffraction pattern, Cu Kα$_1$ radiation, (λ=1.54 Å), for the FC35 clay calcined at 860 ℃ in a brick-fabrication industrial oven. The sample contains muscovite and

quartz. Kaolinite is no longer present and metakaolin is evident as a scattering bump centered at 25 ° (2Θ).

Figure S4. Heat flow traces for PC-FC35-Cc system with increasing amounts of additional gypsum. From the curves, it is inferred that 3 wt% gypsum additional dosage is suitable to have the second calorimetry peak (C_3A-due) well after the first (alite-due) peak.
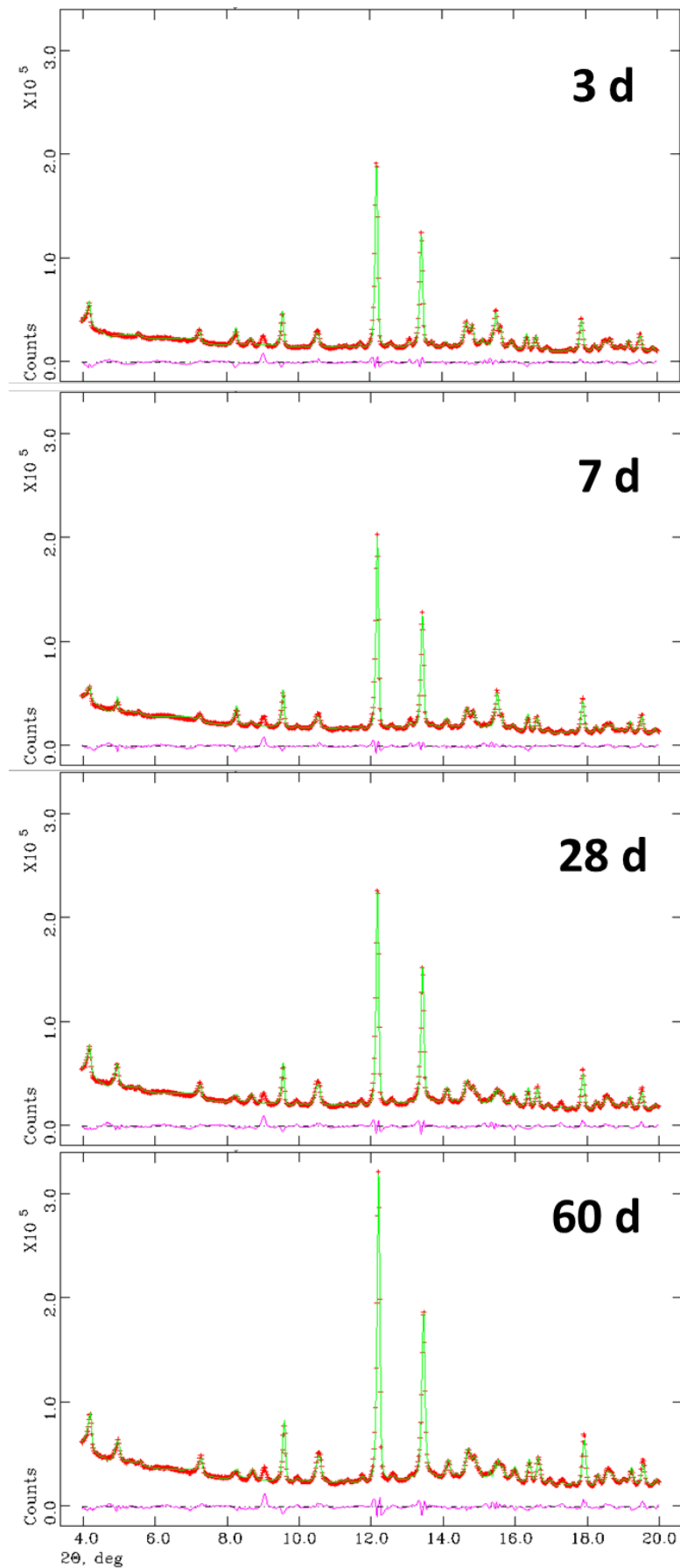
Figure S5. Rietveld plots, Mo-Kα₁ strictly monochromatic radiation (λ=0.71 Å), for the PC-FC35-Cc-G pastes at the indicated hydration ages. The patterns also contain the quartz diffraction peaks, used as internal standard to determine the overall amount of amorphous phase.
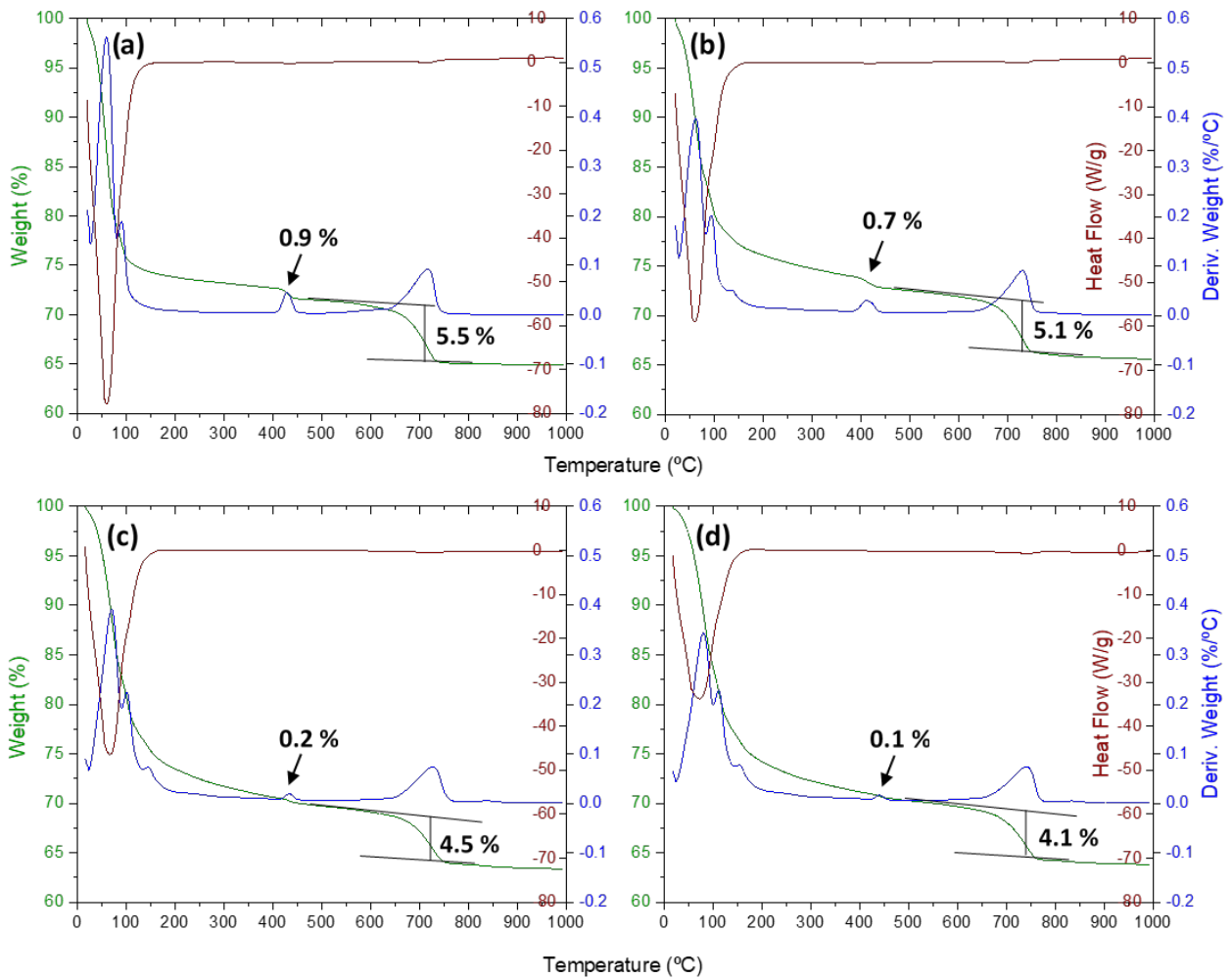
Figure S6. Rietveld plots, Mo-Kα_1 strictly monochromatic radiation (λ=0.71 Å), for the PC-MK-G pastes at the indicated hydration ages. The patterns also contain the quartz diffraction peaks, used as internal standard to determine the overall amount of amorphous phase.

PC-FC35-Cc-G	H$_2$O w.l. (%) / CH wt%	CO$_2$ w.l. (%) / Cc wt%
(a) 2d	0.9 / 3.7	5.5 / 12.5
(b) 7d	0.7 / 3.0	5.1 / 11.6
(c) 28d	0.2 / 0.8	4.5 / 10.2
(d) 60d	0.1 / 0.3	4.1 / 9.3

Figure S7. Thermal analysis traces (green – weight loss; blue – derivative of the weight loss; and brown – heat flow) for the PC-FC35-Cc-G pastes at the studied hydration ages: (a) 2 days, (b) 7 days, (c) 28 days and (d) 60 days.
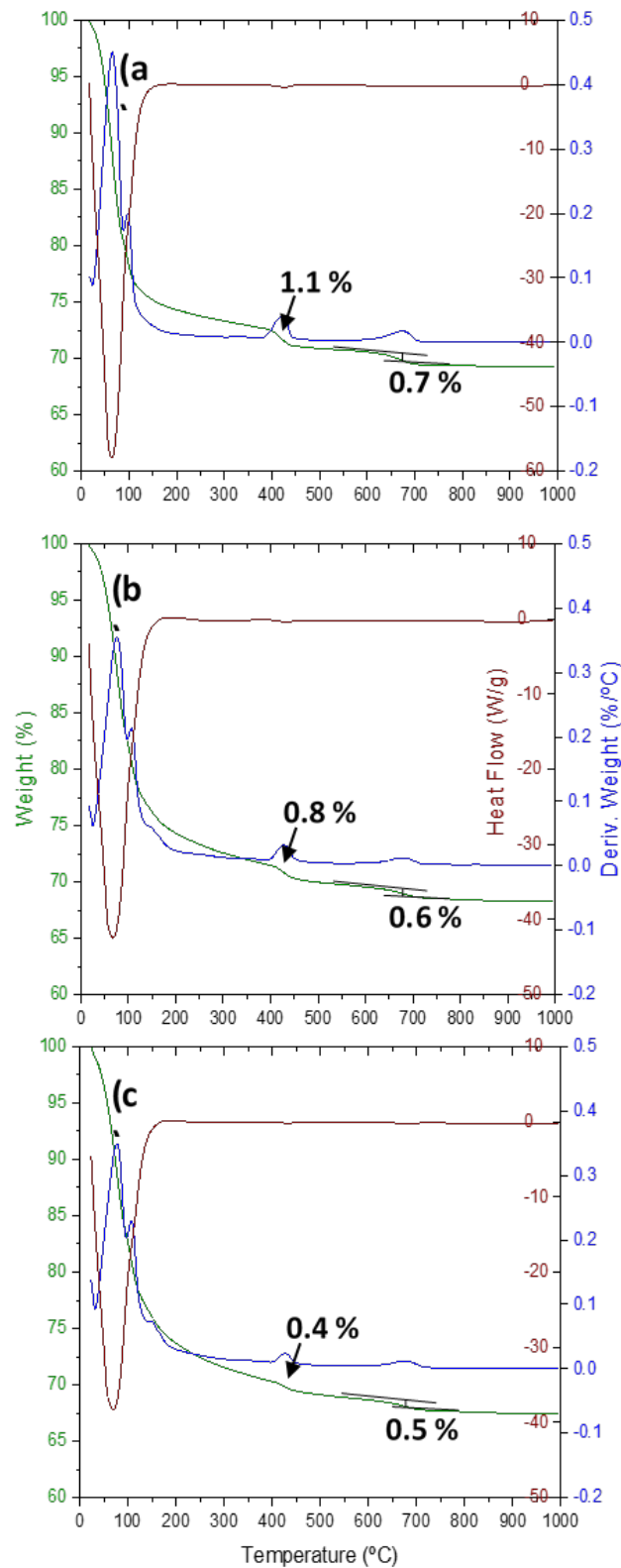
PC-MK-G	H$_2$O w.l. (%) / CH wt%	CO$_2$ w.l(%) / Cc wt%
(a) 2d	1.1 / 4.3	0.7 / 1.7
(b) 7d	0.8 / 3.3	0.6 / 1.4
(c) 28d	0.4 / 1.7	0.5 / 1.2

Figure S8. Thermal analysis traces (green – weight loss; blue – derivative of the weight loss; and brown – heat flow) for the PC-MK-G pastes at the studied hydration ages: (a) 2 days, (b) 7 days and (c) 28 days.
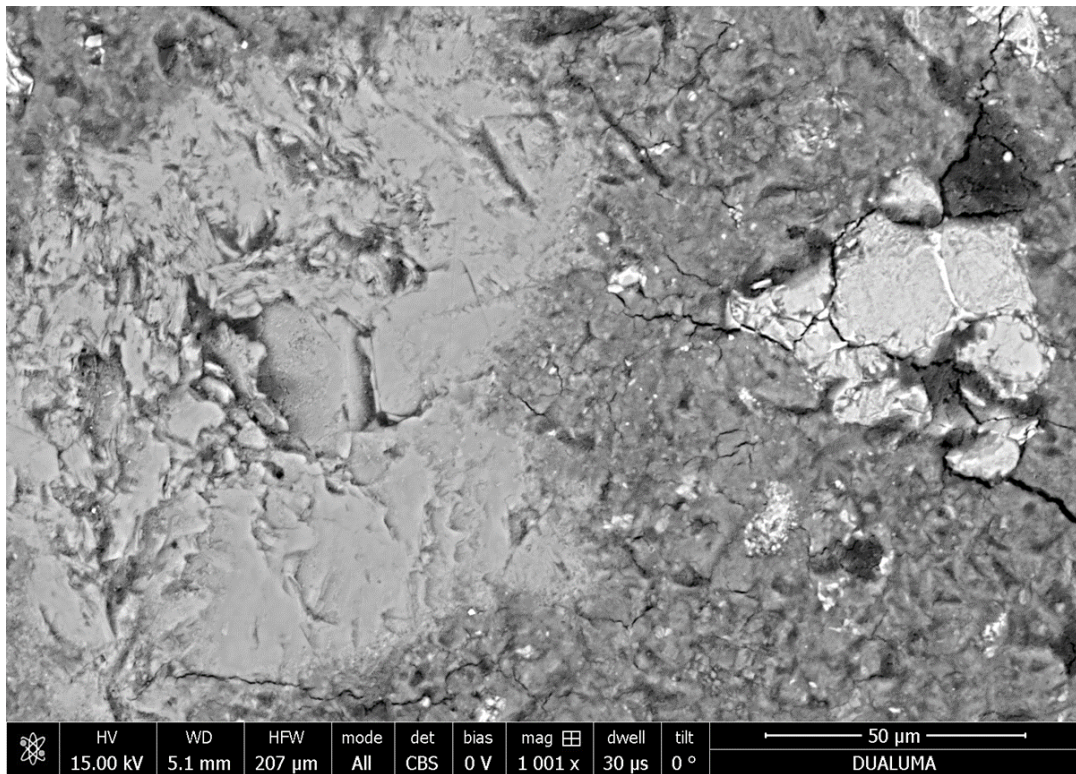
Figure S9. Selected BSE-SEM microphotograph for PC-FC35-Cc-G paste after 28 days of hydration.
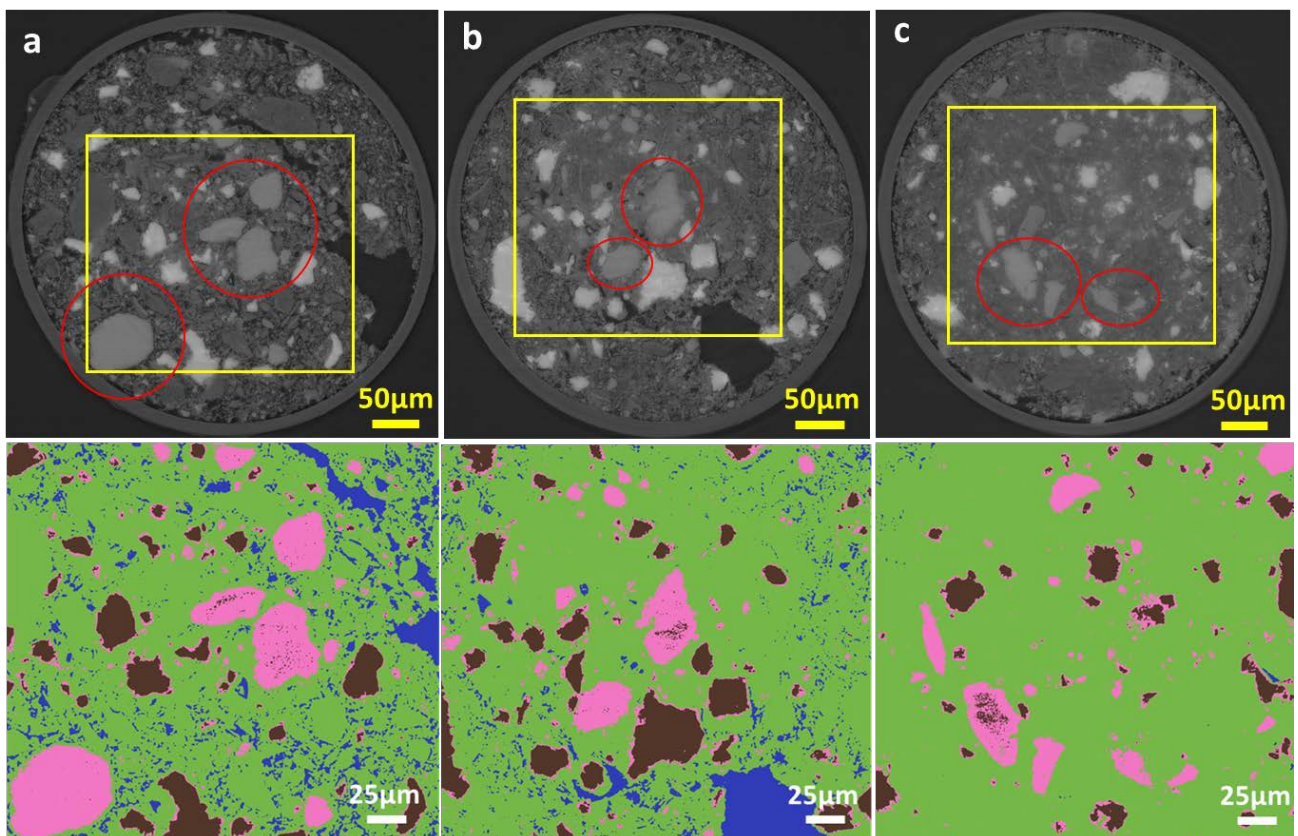

Figure S10. Top row: selected views of the Paganin reconstructed orthoslices for: (a) PC-FC35-Cc-G-7d, (b) PC-FC35-Cc-G-2d and (c) PC-FC35-Cc-G-60d. Calcite particles are highlited in red. Bottom row: segmentation outputs for the regions highlighted with a yellow squares. Pores (blue, $gsv \leq 16,000$), HP (green, $16,000 < gsv \leq 28,500$), Calcite (pink, $28,500 < gsv \leq 33,000$), and UHP (brown, $33,000 < gsv$); gsv=grey scale value.